MECHANICS AND DYNAMICS OF ORBITAL DRILLING OPERATIONS

by

ONUR MERT OZTURK

B.Sc., Istanbul Technical University, Turkey, 2014

A THESIS SUBMITTED IN PARTIAL FULFILLMENT OF

THE REQUIREMENTS FOR THE DEGREE OF

MASTER OF APPLIED SCIENCE

in

THE FACULTY OF GRADUATE AND POSTDOCTORAL STUDIES

(Mechanical Engineering)

THE UNIVERSITY OF BRITISH COLUMBIA

(Vancouver)

May 2017

Abstract

Opening large number of holes takes considerable amount of time during manufacturing and assembly of aircrafts. Traditionally, tools having the same diameter of each hole have been used in drilling which take considerable amount of time for tool change and fixturing. Recently, orbital drilling technology has been introduced to open holes with a single set-up. The combined orbital motion around the hole and helical penetration in axial direction are either given by stationary computer numerically controlled (CNC) machines or hand held, portable heads that are attached to aircraft body with suction pads. Although the tool path and machine were developed, the process mechanics and dynamics have not been modeled to predict cutting forces, torque, power and chatter stability diagrams to identify most productive and safe cutting conditions. This thesis presents mathematical model to simulate the mechanics and dynamics of orbital drilling process.

The mechanics of the process are modeled by identifying the chip thickness distribution along the peripheral and bottom cutting edges of the helical end mills used in orbital drilling, The pitch length of the path, tool and hole diameters, spindle speed, feed and material properties are used in the model which is experimentally proven by comparing predicted and measured cutting forces.

The flexibilities of the orbital drilling head and tool are incorporated to the mechanics model to predict the dynamics of the system. It is shown that the additional delay contributed by orbital motion of the tool can be neglected, and the regenerative delay is dominated by the spindle speed. However, structural dynamic modes of the system need to be oriented along the tangential feed direction since it varies continuously along the orbital path. The chatter stability

of the system has been developed in both frequency and semi-discrete time domains. The experimentally verified stability model considers spindle speed, tool and hole geometries, structural dynamics, material properties and orbital drilling pitch length.

The proposed orbital drilling model allows optimal selection of spindle speed, feed, orbital speed, pitch length and tool diameter for a given work material without overloading the machine and chatter while achieving highest possible material removal rates.

Lay Summary

Drilling operations are widely used in aircraft industry to assemble light structural parts. Traditional drilling requires tools having the same diameter as the hole, hence significant number of drills are needed in production. Additionally, drills cannot be used to open holes with large diameters. The drilling must be followed by boring, which increases cost and production time.

Orbital drilling is an emerging method to open holes with any diameter, which is larger than the tool diameter. Portable, computer controlled orbital drilling heads are clamped to aircraft body with suction pads. End mill with drilling edges at the bottom traverses along the hole circumference while helically penetrating into material along the hole axis.

This thesis presents the mathematical model of the process to predict the chatter vibration free, most productive spindle speed, feed, and pitch length of the process as a function of tool geometry, work material properties and machine's stiffness.

Preface

This thesis presents a product of the research conducted by the author, Onur Mert Öztürk, under the supervision of Professor Yusuf Altintas. This project has been completed in the Manufacturing Automation Laboratory at the University of British Columbia.

I was the lead investigator of the thesis, responsible for conducting the experimental work, developing the algorithms and writing the manuscript. The thesis was proposed, supervised and edited by Professor Yusuf Altintas.

Table of Contents

List of Tables

List of Figures

Nomenclature

a_p	Pitch length of the tool path
dz	Differential axial depth of cut
$D(t)$	Time varying directional matrix
D_H	Intended hole diameter
D_P	Tool Path diameter
D_T	Cutting tool diameter
e	Eccentricity
f_{ax}	Axial linear feed
$f_{\tan}$	Tangential linear feed
$F_{t,\mathrm{b}}$, $F_{r,\mathrm{b}}$, $F_{a,\mathrm{b}}$	Tangential, radial, axial forces on the bottom of the cutting tool
$F_{x,\mathrm{b}}$, $F_{\mathrm{y,b}}$, $F_{\mathrm{z,b}}$	Forces on x, y and z directions on the bottom of the cutting tool
$F_{t,\mathrm{r}}$, $F_{r,\mathrm{r}}$, $F_{a,\mathrm{r}}$	Tangential, radial, axial forces on the periphery of the cutting tool
$F_{x,\mathrm{r}}$, $F_{\mathrm{y,r}}$, $F_{\mathrm{z,r}}$	Forces on x, y and z directions on the periphery of the cutting tool
$\overline{F_{\mathrm{x,b}}}$, $\overline{F_{\mathrm{y,b}}}$, $\overline{F_{\mathrm{z,b}}}$	Average forces on x, y and z directions on the bottom of the cutting tool
J	Tooth index
$K_{tc,\mathrm{b}}, K_{rc,\mathrm{b}}, K_{ac,\mathrm{b}}$	Cutting force coefficients on the bottom of the cutting tool in tangential, radial, axial directions

$K_{te,\mathrm{b}}, K_{re,\mathrm{b}}, K_{ae,\mathrm{b}}$	Edge coefficients on the bottom of the cutting tool in tangential, radial, axial directions
$K_{tc,\mathrm{r}}, K_{rc,\mathrm{r}}, K_{ac,\mathrm{r}}$	Cutting force coefficients on the periphery of the cutting tool in tangential, radial, axial directions
$K_{te,\mathrm{r}}, K_{re,\mathrm{r}}, K_{ae,\mathrm{r}}$	Edge coefficients on the periphery of the cutting tool in tangential, radial, axial directions
n	Spindle Speed [RPM]
n_o	Orbital Speed [RPM]
N	Number of cutting tooth
N_m	Number of natural modes
q	Differential physical displacement vector in time domain
r	Radial engagement length
R_T	Cutting tool radius
R_H	Hole radius
s_{ax}	Axial feed rate
$s_{\tan}$	Tangential feed rate
$X_{Periphery}, Y_{Periphery}$	Periphery of the tool on xy plane
$X_{ToolCenter}, Y_{ToolCenter}$	The position of the tool center on xy plane
w_c	Instantaneous width of chip
α	Ramp angle of the tool path
β	Tool inspection arc radius

β_h	Helix angle of the cutter
Δt	Time interval
Δz	Vertical displacement of tool at each time interval
$\theta(t)$	Rotation of the tool center around hole center [rad]
ξ	Damping ratio
τ	Tooth passing period
τ_0	Time varying delay
Φ_{xx}, Φ_{yy}	Direct FRFs on x and y direction
Φ_{xy}, Φ_{yx}	Cross FRFs
$\emptyset_{st,r}, \emptyset_{ex,r}$	Radial engagement boundaries
ϕ_{pitch}	Pitch angle of the cutting tool
$\phi_{j,r}(k)$	Instantaneous immersion angle
ω	Spindle speed [rad/sec]
ω_c	Chatter frequency
ω_n	Natural frequency
Ω	Orbital speed [rad/sec]
CAD	Computer aided design
CFRP	Carbon fiber reinforced polymers (CFRP)
CFRP/Ti	Carbon fiber reinforced polymers /Titanium
CNC	Computer numerical control
FRF	Frequency response function

STL	Stereolithography
TWE	Tool-Workpiece Engagement
3D	Three dimensional

Acknowledgements

I would like to start with expressing my deepest gratitude to my research supervisor Dr. Yusuf Altintas for his guidance, patience and also belief in me during my studies. I would not have been able to finish this work without his research experience and his continuous support. It was a great privilege of mine working as an assistant under his supervision.

I would like to accentuate my sincere heart-felt thanks to Dr. Doruk Merdol for his guidance and mentorship since the last year of my undergraduate study. Throughout my time in MAL, I had the chance to work with many brilliant people who showed me nothing but kindness. Among them, I would like to thank Alptunç, Coşkun and Deniz for their sincere friendship. During my time in Vancouver I met a lot of special people, among them I would like to thank Kardelen Çalıkıran for making my life better and more enjoyable. Besides, I also would like to thank Can Mahmut Çelebi, my brother by heart, for always sharing my dreams and for always being a solid-funny support, even when we are miles away, since the first day of our high school years.

Last but not least, I have been very fortunate to have my beloved family's unconditional support through my whole life. I would not be able to thank enough my mother Serap Kulalar, my grandmother Emel Kulalar, my uncle Doğan Kulalar and also my grandfather Şinasi Kulalar, who passed away many years ago. Now, as a young man I see their sacrifices on another level which makes me nothing but grateful. My so-called success in life is just a small reflection of the love, kindness and compassion given by my family. Including this work, all of my past and future successes are dedicated to them.

To my mother,

who taught me how to dream

Chapter 1: Introduction

Aircraft parts are mainly assembled by riveting or bolting them through holes opened with drilling operations. A typical mid-size aircraft may have over a million holes, hence the process is highly time consuming and costly. While holes with small diameter are opened through twist or indexed drills, and holes with large diameter have been opened combination of drilling and boring on large machine tools. Orbital drilling is a new technology which allows opening of medium to large diameter holes on the aircraft body directly during the assembly. The portable, computer numerical controlled (CNC) drilling head is attached to aircraft body through suction, and the drilling head follows an orbital – helical motion to open and enlarge the hole by an end milling process. The operation has been found successful in drilling aluminum, titanium and composite parts in aerospace industry. In orbital drilling, an end mill moves along a three dimensional helical tool path by cutting at its periphery and bottom to open the hole. The cutting forces on both sections may excite the structural dynamics of the machine tool head during the operation. If the process parameters are not selected correctly, the flexibility of the orbital drilling head, spindle and end mill may experience severe chatter and large deflections which may destroy the costly aircraft parts during assembly. This thesis presents modeling the mechanics and dynamics of the orbital drilling process to predict the cutting forces, dimensional surface errors and chatter stability. The mathematical simulation model is intended for optimal selection of tool geometry, orbital and tangential feeds, and spindle speeds without causing chatter and overloading of the machine and cutting. .

The thesis is organized as follows:

Chapter 2 summarizes the related background and the review of the literature in orbital drilling.

In Chapter 3, the mechanics of orbital drilling operations is presented. A numerical method to identify tool-workpiece engagements (TWE) is introduced, and compared against the previous approaches [11]. The cutting force coefficients of the bottom part of the end mill are identified mechanistically, and the coefficient for the peripheral side are predicted from the orthogonal cutting parameters. The mechanics of orbital drilling have been experimentally validated by comparing the predicted and measured cutting forces.

Chapter 4 is dedicated to the chatter stability of the orbital drilling operation. The regenerative time delay has two components: One is caused by the spindle speed while the other is contributed by the orbital – helical feed motion of the tool. The mathematical modeling of the orbital – helical motion has a negligible contribution to regenerative delay which is dominated by the spindle speed. The stability is reduced to regular end milling process but with feed direction dependent structural dynamics. Chatter stability of the operation is solved in semi discrete time domain and frequency domains. Nyquist stability criterion is used for frequency domain approach considering the radial engagement boundaries of the end mill. Three dimensional stability lobes are predicted as a position of the tool along the orbital path, spindle speed and pitch lengths of the tool path. The stability models are verified experimentally.

The thesis is concluded in Chapter 5, summarizing the contributions of the thesis and future research directions.

Chapter 2: Literature Review

2.1 Overview

Hole machining is one of the most dominating in aerospace industry. While regular twist drilling operations have been widely studied and used, the orbital drilling is a new process and emerged during the last decade. Orbital drilling has shown a great capability of machining burr free and high quality holes in different types of aerospace materials. The mechanics and dynamics of twist drilling, where the drill rotates and moves only in axial direction, have been widely studied in the past. The prediction of drilling forces [20, 21], forced [22, 23] and self-excited chatter vibrations [24, 25, 26] have been widely published. However, the mechanics and dynamics of orbital drilling, where the tool follows an orbital and helical path to open and enlarge the hole, has not been studied widely to predict the cutting forces, chatter free cutting conditions and dimensional hole quality. The objective of this thesis is to predict the cutting forces and chatter stability diagrams to identify most productive and safe cutting conditions. This chapter presents the review of the orbital drilling literature.

2.2 Application and Experimental Investigation of Orbital Drilling Operations

The major concern of the hole drilling processes is the dimensional quality of the hole while using tool geometry and cutting conditions which yield to highest productivity.

Early studies on the orbital drilling process mostly focused on the applicability of the operation and its potential to replace conventional, twist drilling process. The first study by

Lindqvist et al. [1] from Navator Company of Sweden showed that the orbital drilling process is capable of eliminating delamination while machining holes on carbon sandwich structures for aerospace applications. They designed a novel portable, orbital drilling system attached to aircraft body to drill holes during the assembly, and demonstrated the applicability of the process with test trials.

The academic investigations followed the introduction of orbital drilling concept. Kihlman et al. [2] compared the cutting forces in orbital drilling and conventional drilling process by conducting experiments. They showed that the orbital drilling leads to lower axial cutting forces than the conventional drilling process. Lindqvist and Kihlman [3] from Navator experimentally proved that the orbital drilling produces holes with higher surface quality and in comparison to conventional drilling. Furthermore, the work of Whinnem [4] on Boeing 787 demonstrated that the orbital drilling process can create holes without burr which leads to less scrap rate in producing costly aircraft parts. Iyer et al. [5] showed that H7 quality holes on AISI D2 hardened tool steel can be opened with orbital drilling with a surface finish of 0.3 μm, experimentally. The orbital drilling allows the opening of holes with different diameter with the same tool diameter [6]. Furthermore, the same cutting tool can be used for finish machining of the hole, hence the number of post-processes (i.e. boring) for opening the borehole is reduced. The observed reduction in cutting forces led to the use of industrial robots or similar light weight but mobile structures for portable orbital drilling operations [7]. A portable orbital drilling unit on a robot is shown in Figure 2.1.

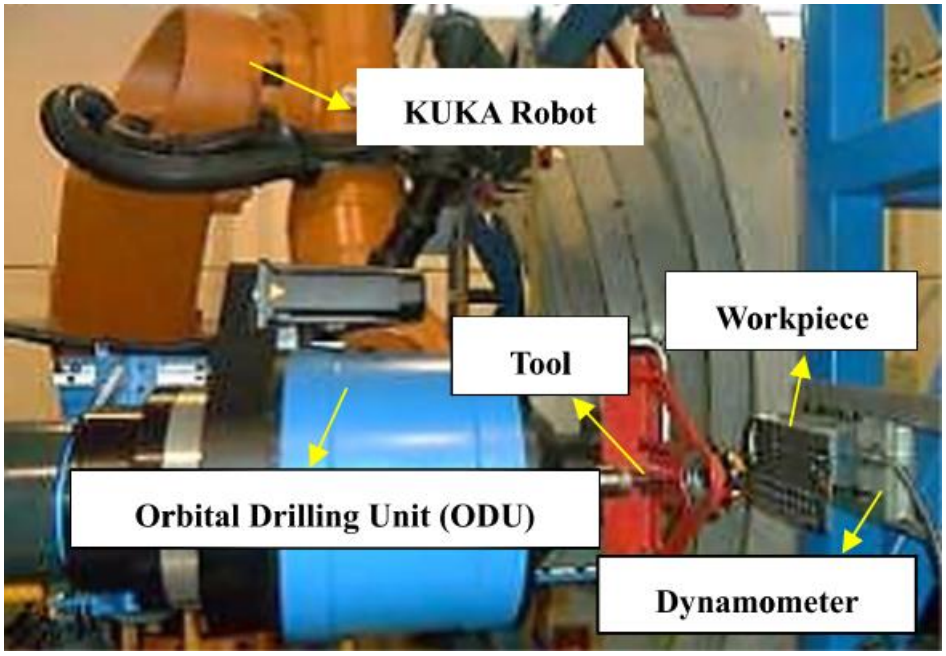

Figure 2.1 Robotic orbital drilling unit. Taken from [10].

Orbital drilling is highly used in machining of carbon fiber reinforced polymers (CFRP) and carbon fiber reinforced polymers/titanium (CFRP/Ti) alloy stacks in aerospace industry. Since the process results in lower drilling forces compared to conventional drilling, the process temperature is expected to be lower [9]. Orbital drilling also led to less low burr formation and reduced delamination in machining CFRP or CFRP/Ti relative to conventional drilling [6,8,9]. In a recent work [10], researchers investigated the effects of orbital drilling on the hole diameter variation and roundness of CFRP/Ti stacks. The outcome of their work showed that hole and tool diameter ratio has a greater impact on the roundness of the CFRP layer.

All of the articles cited in this section are based on experimental trials without providing model based, analytical reasoning.

2.3 Mechanics and Dynamics of Orbital Drilling Operations

The kinematics model of orbital drilling was first studied by Brinksmeier et al. [11], which led to the prediction of varying tool- workpiece engagements as a function of tool and hole diameters, the pitch length of helical - downward motion along the tool path. The model led to the prediction of chip geometry generated by cylindrical flat end mills as shown in Figure 2.2. Li and Liu [12] created a simulation model based on Z-mapping to simulate three-dimensional (3D) surface topography of the finished hole produced by orbital drilling process.

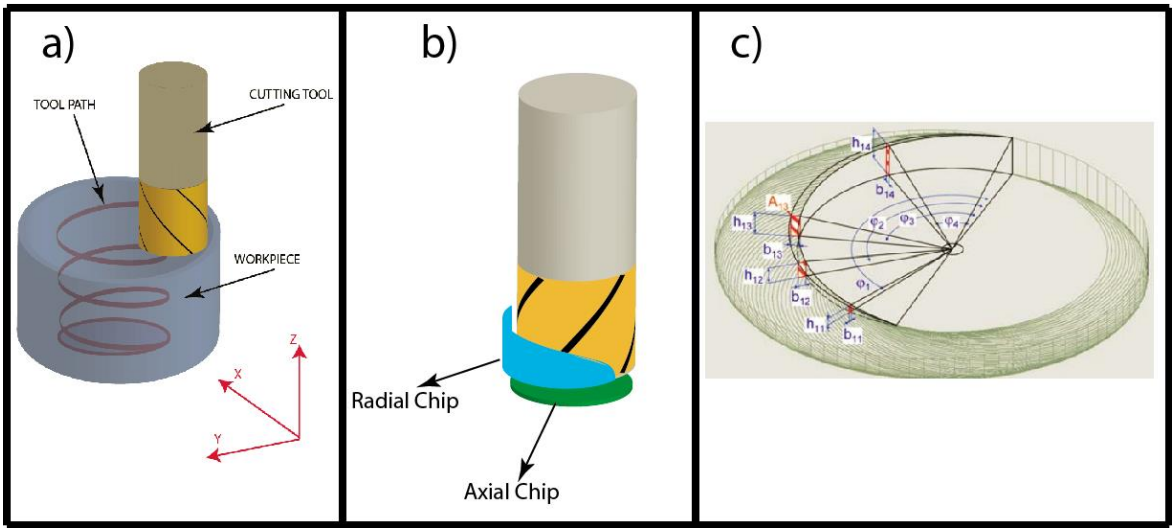

Figure 2.2 a) Orbital drilling process b) Undeformed chip geometries during orbital drilling c) topography of the hole ground and the cross section of undeformed chip of the radial cut as a function of immersion angle. Taken from [11]

Liu et al. [13] predicted orbital drilling forces as a function of spindle speed, helical feed, radial and axial cutting depth, and cutter geometry. Wang et al. [14] identified the cutting force coefficients mechanistically from a series of orbital drilling tests conducted on titanium. In a recent study, Meyer et al. [15] considered complex tool geometries in modeling orbital drilling

forces by considering the chip geometry and forces generated by the bottom and radial parts of the tool. The differences between the predicted and measured forces are attributed to the indentation of the bottom part of the end mill into the work material.

The prediction of vibrations, hole surface quality and chatter free depth, speed and pitch length require the dynamic model of orbital drilling.

The circular and thread milling operations have similarities with orbital drilling. They have two time delays which are functions of spindle speed and orbital motion. Kardes and Altintas presented a stability model of circular milling which resembles orbital milling but without axial motion [17]. They applied zero order solution of Altintas and Budak [27] and Finite Time model of Bayly et al. [28] in solving the stability. Thread milling has a path similar to orbital milling but with cutting edges similar to thread profile. Wan and Altintas [18] presented both mechanics and chatter stability models to predict the thread milling process. Dual time delay is considered in solving the stability of operations which are governed by coupled, time periodic, delayed differential equations.

Li et al. [16] presented the only study to predict the chatter stability diagrams, i.e. critical depth of cut versus spindle speed, in orbital milling. They assumed the worst engagement conditions, i.e. slotting or peripheral milling, and applied Altintas and Budak's zero order stability law to simplified orbital drilling process which does not consider varying engagement and dynamic flexibilities along the tool path.

The TWEs are analytically calculated from the kinematics model proposed by Brinksmeier et al. [11]. The engagement conditions are used to describe the chip thickness distribution at the periphery and bottom edges of the helical end mill along the orbital tool path. The cutting forces are predicted as a function of chip thickness distribution. The effect of lateral

vibrations of the flexible tool on the regenerative, dynamic chip thickness is modeled as a function of tool and hole diameters, pitch length of the orbital motion, and feed. The frequency response functions (FRF) of tool structure are projected into the feed and normal directions along the orbital path. The chatter stability of the process is solved by applying the zero order stability law of Altintas and Budak [27] in frequency domain. The chatter stability is also solved in semi-discrete time domain proposed by Insperger and Stepan [19].The linear, semi discrete time model can also be used to predict the cutting forces and vibrations along the tool path [29].

In summary, this thesis presents integrated mechanics and dynamics models of orbital drilling process. The proposed models are experimentally proven.

Chapter 3: Mechanics of Orbital Drilling Operations

3.1 Introduction

Orbital drilling is used to open large holes, especially common in aircraft fuselage manufacturing. The cutting tool follows a 3D helical toolpath with the combination of rotational and axial motions as shown in Figure 3.1.

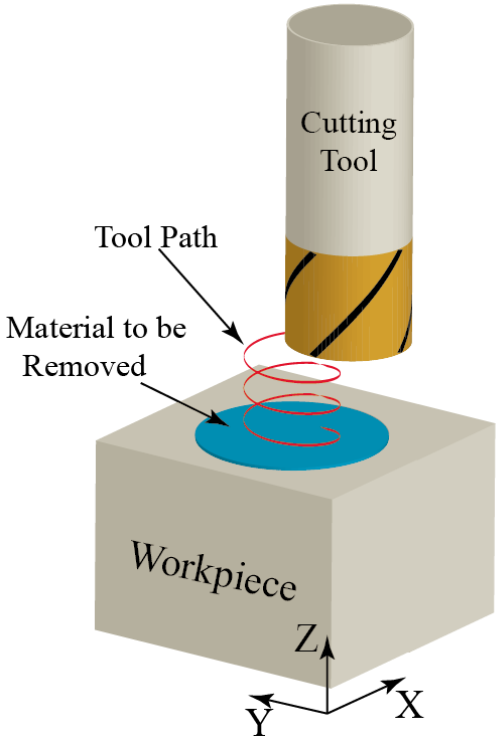

Figure 3.1 Illustration of orbital drilling

This process can be considered as a combination of circular and plunge milling rather than drilling, since the cutting occurs both at the periphery and the bottom part of the tool. The

engagement conditions in orbital drilling can be separated into three different regions as shown in Figure 3.2.

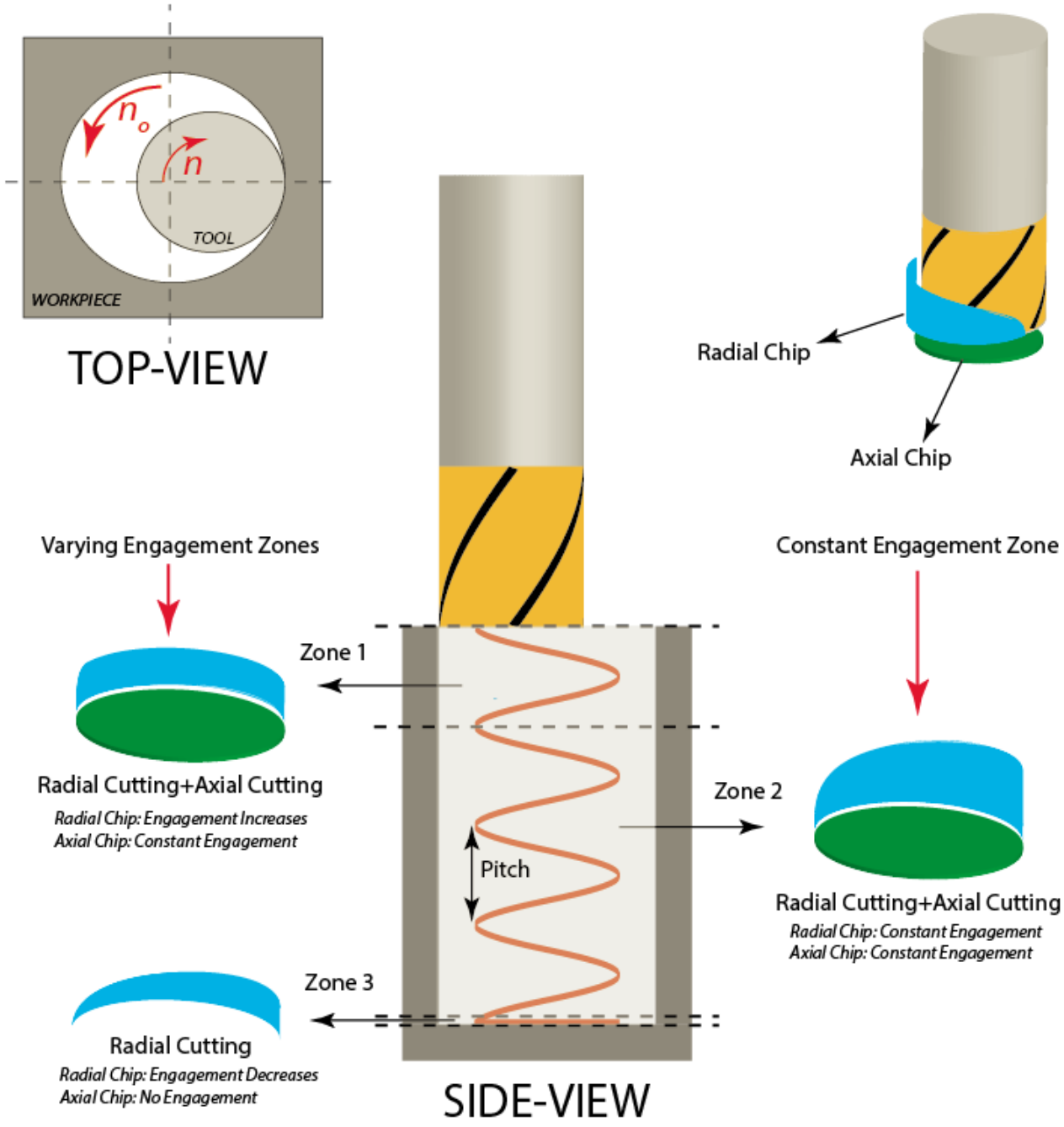

Figure 3.2 Engagement zones in orbital drilling

In this chapter an analytical engagement model from the literature is presented. A model to evaluate engagement conditions is introduced, and its results are compared against the values predicted by computationally costly, generic commercial software (Moduleworks). The kinematics and TWE models are used to evaluate the chip geometry generated during orbital drilling, which is needed for modeling the mechanics of the cutting process. The mechanics of orbital drilling process have been developed, and experimentally proven by comparing the predicted and experimentally measured cutting forces.

3.2 Geometric Modelling of Tool and Workpiece Intersection

Engagement conditions during orbital drilling operation vary as the tool penetrates and leaves the work material, since both radial and axial edges of the cutting tool remove material from the workpiece. While the cutting tool moves along the 3D helical toolpath, axial part of the tool engages with the workpiece first followed by the radial edges (Figure 3.2.). The axial part of the tool has full contact with the workpiece material in regions 1 and 2. However, the radial engagement conditions change in region 1 where the cutting tool rotates 360 degrees around the center of the hole. The engagement area on the radial part of the tool increases as the tool plunges into the workpiece until the pitch length of the tool path is travelled. After tool finishes the first 360 degrees of rotation inside the workpiece, the engagement areas on both radial and axial cutting edges stay constant although the radial engagement boundaries, the entry $\emptyset_{st,r}$ and exit $\emptyset_{ex,r}$ angles of the tool change along the longitudinal direction of the cutter. In region 3, the tool makes the last 360 degrees of rotation around the center of the hole on xy plane without a plunge motion which resembles circular milling. The engagement conditions vary significantly

in region 3. The radial engagement boundaries for slot milling and orbital drilling operations are shown in Figure 3.3 to highlight the differences.

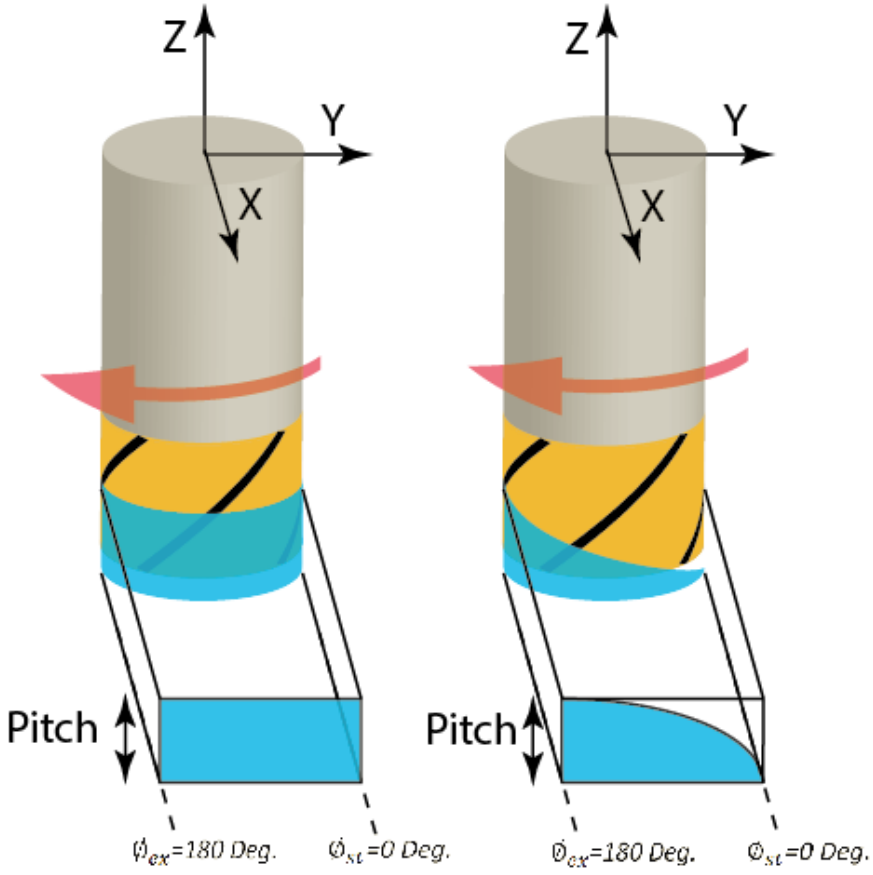

Figure 3.3 Comparison of radial engagements, left slot milling case, right orbital drilling case

3.2.1 Modelling of the Radial Engagement

Brinksmeier et al. [11] presented the geometric engagement of cylindrical end mills zone 2 of orbital milling where radial engagement boundaries stay constant. The intended hole diameter D_H, cutting tool diameter D_T, and the pitch length of the tool path a_p are used in the engagement model.

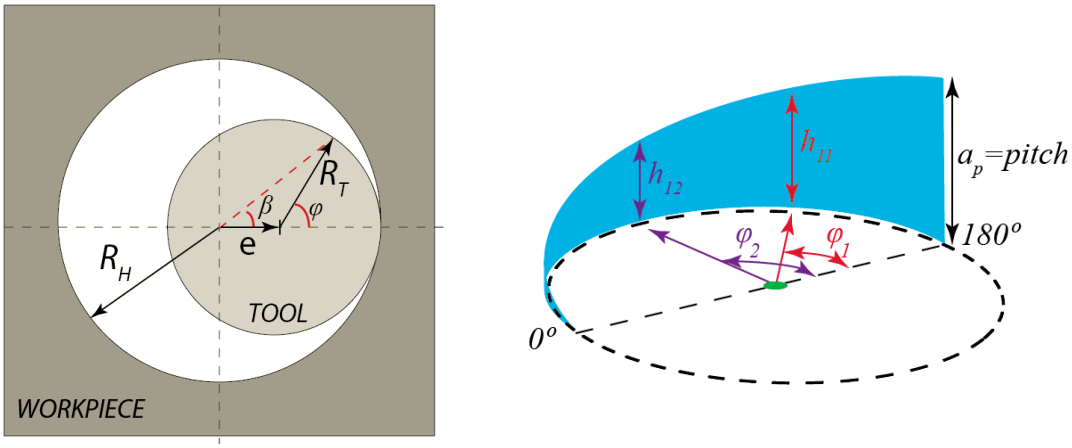

Figure 3.4 Graphic for the calculation radial engagement condition

The eccentricity (e) of the tool center from the hole center is,

$$R_T = \frac{D_T}{2}, \quad R_H = \frac{D_H}{2}, \qquad e = R_H - R_T \tag{3.1}$$

The tool inspection arc angle β (Figure 3.4) is,

$$\beta = \arcsin \frac{\sqrt{R_T^2 - \left(R_T \cos\varphi\right)^2}}{\sqrt{\left(R_T \sin\varphi\right)^2 + \left(e + R_T \cos\varphi\right)^2}} \tag{3.2}$$

The cutting tool engagement boundaries change along the circumference of the tool (Figure 3.4). The depth of the radial chip along the tool circumference is given as:

$$h_{1i} = a_p \left(1 - \frac{\beta}{\pi}\right) \tag{3.3}$$

The radial engagement area along the circumference of the cylindrical end mill changes as the tool rotates around the center of the hole in zone 1 and 3, which is modeled here.

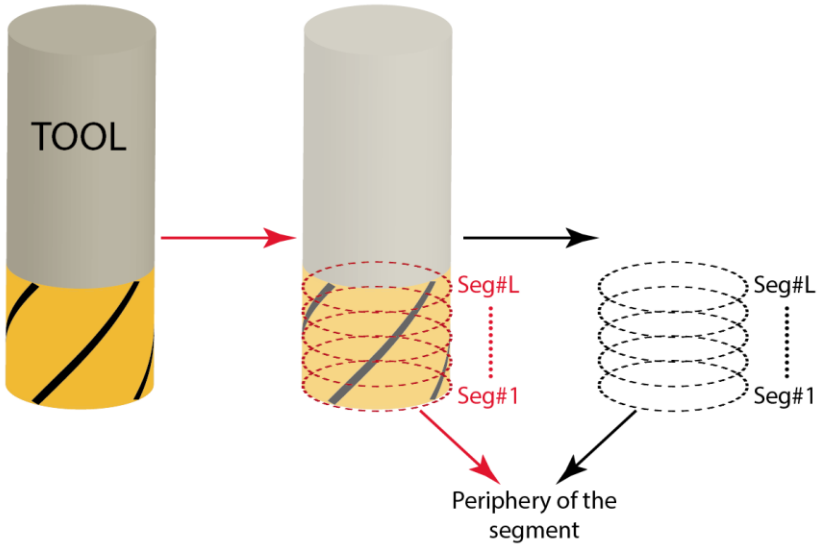

Figure 3.5 Discretization of tool periphery along the axial direction of the tool

. Since the periphery of the end mill does not change along the axial direction of the cylindrical tool, its orbital motion can be projected on xy plane. If the rigid body motion of the tool is discretized at discrete time intervals Δt, the position of the tool center can be found on xy plane as:

$$\begin{aligned} X_{ToolCenter}(t) &= e \cdot \cos\theta(t) \\ Y_{ToolCenter}(t) &= e \cdot \sin\theta(t) \\ \theta(t) &= \Delta t \cdot \Omega \end{aligned} \tag{3.4}$$

where Ω is the orbital speed [rad/sec] and $\theta(t)$ is the rotation of the tool center around hole center in [rad]. Vertical displacement of the tool at each time interval is Δz,

$$\Delta z = \Delta t \cdot f_{ax} \tag{3.5}$$

where f_{ax} is the axial feed. Tool's periphery at each time step can be evaluated as follows.

$$\begin{aligned} X_{Periphery}(t) &= X_{ToolCenter}(t) + R_T \cdot \cos\varphi \\ Y_{Periphery}(t) &= Y_{ToolCenter}(t) + R_T \cdot \sin\varphi \\ &where,\ 0 \le \varphi \le 2\pi \end{aligned} \tag{3.6}$$

By considering the tool's previous positions on both vertical and horizontal planes, as well as on its periphery, the radial engagement at each time step can be predicted with a line intersection algorithm. The intersection points represent the starting points of the radial engagement $\emptyset_{st,q}$, along the tool's axial direction. The engagement area along the tools feed direction is shown in Figure 3.6.

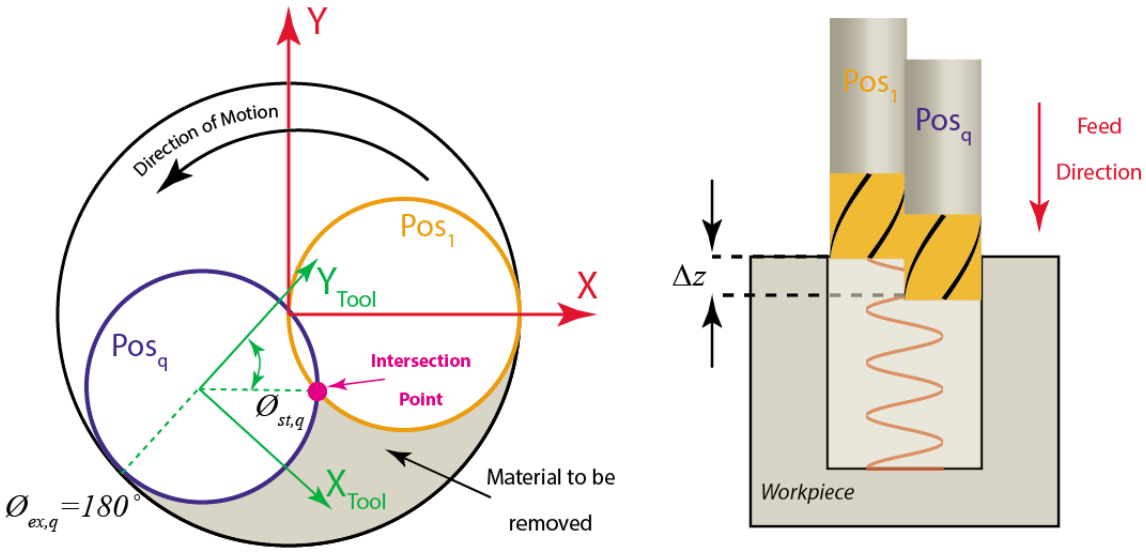

Figure 3.6 Tool motion on vertical (right) and horizontal (left) planes

3.2.2 Comparison of the Engagement Models

The proposed radial engagement of the tool with the workpiece during the orbital drilling is compared against commercial graphics system Moduleworks.

In Moduleworks which is a module within UBC's virtual machining system (MACHPRO), the TWEs are calculated at discrete points of the tool path. The engagement boundaries, the stereolithography (STL) file of the raw material geometry and NC tool path are used as inputs in calculating the engagements. Engagement information is extracted at user defined, constant

sampling distances along the tool path. A sample orbital drilling process (a), the radial engagement area of an end mill at a point where the tool is in zone 2 (b), and the corresponding hole shape (c) are shown in Figure 3.7.

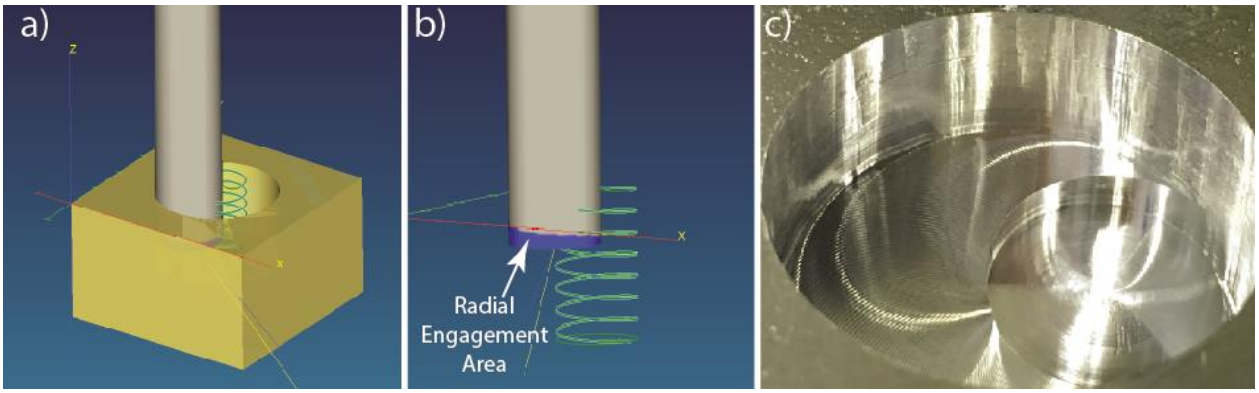

Figure 3.7 a) Virtual orbital drilling on ,MACHPRO , b) Radial engagement mapped on the end mill, c) Workpiece after end mill leaves the workpiece in zone2

The radial engagement on the end mill is projected to two dimensional plane where horizontal and vertical axes represent the immersion angle and the axial depth of chip, respectively. A comparison of engagement maps generated by Moduleworks in MACHPRO and proposed analytical models are shown in Figure 3.8 where the results are in good agreement.

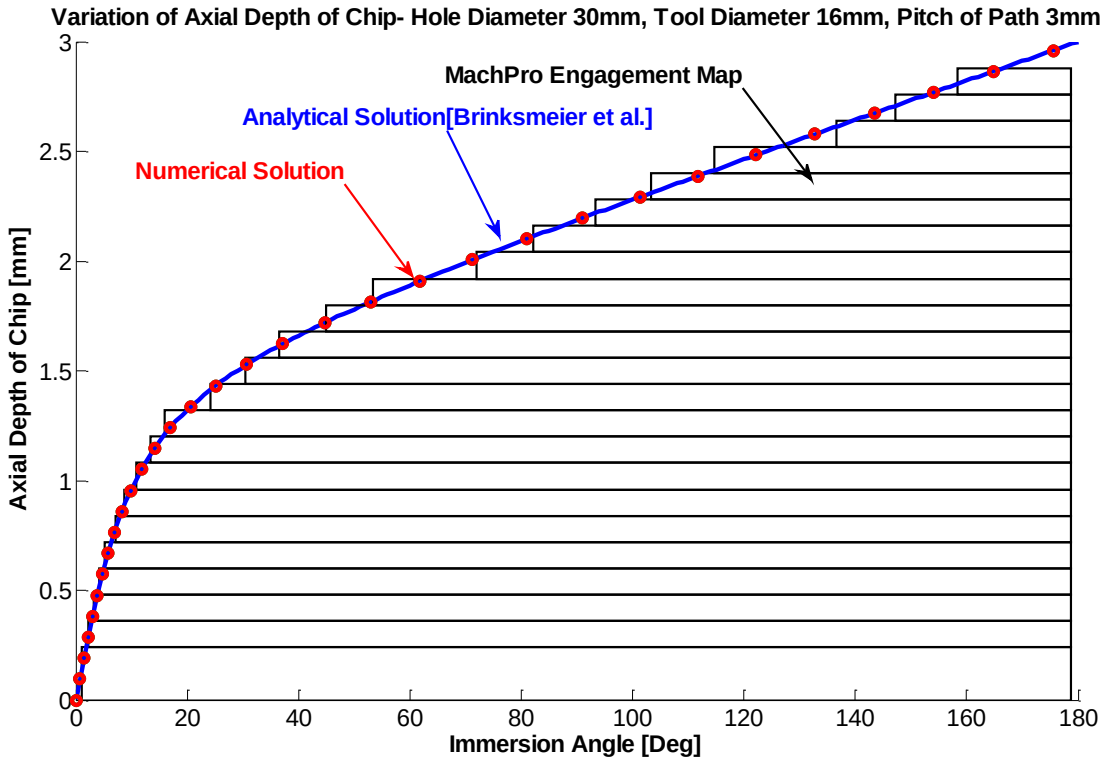

Figure 3.8 Comparison of the radial engagement boundaries. Cutting conditions: Hole Diameter D_H = 30 mm, tool Diameter D_T = 16 mm, pitch length of the tool path a_p = 3 mm, spindle speed n = 1000 rpm, orbital speed n_o = 6 rev/min, s_{tan}= 0.1319 mm/rev/tooth, s_{ax} = 0.009 mm/rev/tooth.

Moduleworks is based on the STL model of the part and tool, hence the resolution of STL mesh greatly affect the accuracy of evaluating engagement maps. Hence, Moduleworks cannot predict the engagements accurately, if the tool diameter is very small. The proposed engagement map solution is based on the analytical, geometric models of the cylindrical end mill and the hole diameter, hence it is independent of mesh size in STL models of the tool and the part.

3.3 Mechanics of Orbital Drilling

Orbital drilling can be considered as a combination of plunge and circular milling operations. The cutting process at the bottom part of the end mill can be considered as plunge milling, whereas the process at the cylindrical surface resembles the circular milling process. The mechanics of the circular milling was investigated by Kardes and Altintas [17]. They considered the varying engagement conditions of the solid end mill and workpiece along the circular – trochoidal tool path. Ko and Altintas [30] presented mechanics of plunge milling by utilizing the chip generated by the axially penetrating end mill as it rotates.

In addition to the engagement geometry presented in the previous section, the mechanics model require the identification of cutting force coefficients, chip thickness and cutting force model which are presented below.

3.3.1 Identification of Cutting Force Coefficients at the Bottom Part of the End Mill

The accuracy of the cutting force estimation significantly depends on the accuracy of cutting force coefficients. Unlike the geometry of cutting edges on the periphery of end mills, the manufacturers do not provide much information about the geometry of flutes at the bottom of the tool. Since it is also difficult to measure the bottom geometry on the standard tool microscopes, the cutting force coefficients need to be identified from the cutting experiments. During the orbital drilling process bottom part of the end mill plunges into the material like a drill, hence the

chip thickness distribution and the corresponding cutting force coefficients need to be identified from the geometry of cut shown in Figure 3.9.

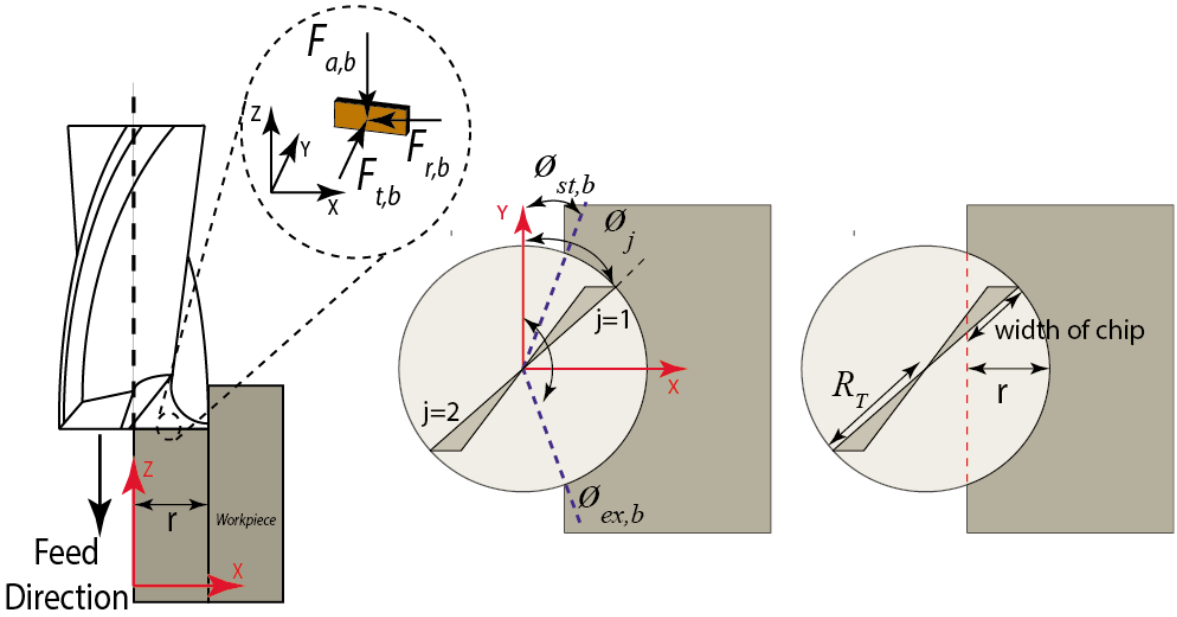

Figure 3.9 Plunge milling geometry

The instantaneous width of chip w_c is given by.

$$w_c = R_T - \left\{ \frac{R_T - r}{\cos\left(90 - \phi_j\right)} \right\} \tag{3.7}$$

where r is the radial engagement length. The tangential ($F_{t,\mathrm{b}}$), radial ($F_{r,\mathrm{b}}$) and axial ($F_{a,\mathrm{b}}$) forces caused by the plunge milling are expressed as a function of chip area ($h_{ax} w_c$) and cutting edge contact length (w_c):

$$\begin{aligned} F_{t,\mathrm{b}} &= \left\{ K_{tc,\mathrm{b}} \cdot h_{ax} + K_{te,\mathrm{b}} \right\} \cdot w_c \\ F_{\mathrm{r,b}} &= \left\{ K_{rc,\mathrm{b}} \cdot h_{ax} + K_{re,\mathrm{b}} \right\} \cdot w_c \\ F_{\mathrm{a,b}} &= \left\{ K_{ac,\mathrm{b}} \cdot h_{ax} + K_{ae,\mathrm{b}} \right\} \cdot w_c \end{aligned} \tag{3.8}$$

Where h_{ax} is chip thickness and equal to axial feed rate $h_{ax} = s_{ax}$, $\{K_{tc,\mathrm{b}}, K_{rc,\mathrm{b}}, K_{ac,\mathrm{b}}\}$ and $\{K_{te,\mathrm{b}}, K_{re,\mathrm{b}}, K_{ae,\mathrm{b}}\}$ are the cutting and edge force coefficients in tangential, radial and axial directions, respectively.

The tools coordinate and global coordinate systems are coincided. The cutting forces on all teeth are transformed to x,y and z directions as:

$$\begin{aligned} F_{x,\mathrm{b}} &= \sum_{j=1}^{N} \cdot \left\{ -\left\{ K_{tc,\mathrm{b}} \cdot h_{ax} \cdot w_c + K_{te,\mathrm{b}} \cdot w_c \right\} \cdot \cos\phi_j - \left\{ K_{rc,\mathrm{b}} \cdot h_{ax} \cdot w_c + K_{re,\mathrm{b}} \cdot w_c \right\} \cdot \sin\phi_j \right\} \\ F_{y,\mathrm{b}} &= \sum_{j=1}^{N} \left\{ \left\{ K_{tc,\mathrm{b}} \cdot h_{ax} \cdot w_c + K_{te,\mathrm{b}} \cdot w_c \right\} \cdot \sin\phi_j - \left\{ K_{rc,\mathrm{b}} \cdot h_{ax} \cdot w_c + K_{re,\mathrm{b}} \cdot w_c \right\} \cdot \cos\phi_j \right\} \\ F_{z,\mathrm{b}} &= \sum_{j=1}^{N} \left\{ K_{ac,\mathrm{b}} \cdot h_{ax} + K_{ae,\mathrm{b}} \right\} \cdot w_c \end{aligned} \quad (3.9)$$

Instead of using orthogonal to oblique cutting transformation [31], the mechanistic prediction of cutting coefficients for the bottom edges of the tool is employed. The average cutting forces per tooth period are measured while the axial feed rate is varied during each experiment with constant immersion conditions.

$$F_{avg} = \frac{1}{\phi_{pitch}} \int_{\phi_{st}}^{\phi_{ex}} F\left(\phi_j\right) d\phi \quad (3.10)$$

Average forces on each axis can be evaluated as:

$$\begin{aligned} \overline{F_{x,\mathrm{b}}} &= -\frac{N}{2\pi} \delta_1 \left\{ K_{tc,\mathrm{b}} \cdot h_{ax} + K_{te,\mathrm{b}} \right\} - \frac{N}{2\pi} \delta_2 \left\{ K_{rc,\mathrm{b}} \cdot h_{ax} + K_{re,\mathrm{b}} \right\} \\ \overline{F_{y,\mathrm{b}}} &= \frac{N}{2\pi} \delta_2 \left\{ K_{tc,\mathrm{b}} \cdot h_{ax} + K_{te,\mathrm{b}} \right\} - \frac{N}{2\pi} \delta_1 \left\{ K_{rc,\mathrm{b}} \cdot h_{ax} + K_{re,\mathrm{b}} \right\} \\ \overline{F_{z,\mathrm{b}}} &= \frac{N}{2\pi} \delta_3 \left\{ K_{ac,\mathrm{b}} \cdot h_{ax} + K_{ae,\mathrm{b}} \right\} \end{aligned} \quad (3.11)$$

Where δ_1, δ_2 and δ_3 are;

$$\delta_1 = \int_{\phi_{st}}^{\phi_{ex}} \cos\phi_j \cdot \left(R_T - \left(\frac{R_T - r}{\cos\left(90 - \phi_j\right)} \right) \right) d\phi$$
$$\delta_2 = \int_{\phi_{st}}^{\phi_{ex}} \sin\phi_j \cdot \left(R_T - \left(\frac{R_T - r}{\cos\left(90 - \phi_j\right)} \right) \right) d\phi \quad (3.12)$$
$$\delta_3 = \int_{\phi_{st}}^{\phi_{ex}} \left(R_T - \left(\frac{R_T - r}{\cos\left(90 - \phi_j\right)} \right) \right) d\phi$$

In order to obtain cutting coefficients associated with one tooth, intermittent plunge milling tests have been modeled with $r = R_T$, $\emptyset_{ex,b}$ = 180° and $\emptyset_{st,b}$ = 0°. The corresponding average forces can be expressed as:

$$\overline{F_{\mathrm{x,b}}} = -\frac{NR_T}{\pi}\left\{K_{rc,\mathrm{b}} \cdot h_{ax} + K_{re,\mathrm{b}}\right\}$$
$$\overline{F_{\mathrm{y,b}}} = \frac{NR_T}{\pi}\left\{K_{tc,\mathrm{b}} \cdot h_{ax} + K_{te,\mathrm{b}}\right\} \quad (3.13)$$
$$\overline{F_{\mathrm{z,b}}} = \frac{NR_T}{2}\left\{K_{ac,\mathrm{b}} \cdot h_{ax} + K_{ae,\mathrm{b}}\right\}$$

The cutting coefficients associated with the bottom part of the tool can be calculated by following:

$$K_{rc,\mathrm{b}} = -\frac{\pi\overline{F_{\mathrm{xc,b}}}}{NR_T}, K_{re,\mathrm{b}} = -\frac{\pi\overline{F_{\mathrm{xe,b}}}}{NR_T}$$
$$K_{tc,\mathrm{b}} = \frac{\pi\overline{F_{\mathrm{yc,b}}}}{NR_T} =, K_{te,\mathrm{b}} = \frac{\pi\overline{F_{\mathrm{ye,b}}}}{NR_T} \quad (3.14)$$
$$K_{ac,\mathrm{b}} = \frac{2\overline{F_{\mathrm{zc,b}}}}{NR_T}, K_{ae,\mathrm{b}} = \frac{2\overline{F_{\mathrm{ze,b}}}}{NR_T}$$

Half plunge milling tests were carried at 5 different axial feed rates at 1000 rpm and the experiment parameters are given on the Table 3.1.

Table 3.1 Axial feed rates and average forces of half plunge milling tests

	Exp. 1	**Exp. 2**	**Exp. 3**	**Exp. 4**	**Exp. 5**
Axial Feed Rate [mm/rev/tooth]	0.005	0.020	0.040	0.060	0.080
Average Forces on X axis [N]	-1.16	-12.92	-24.82	-34.05	-41.55
Average Forces on Y axis [N]	67.35	144.6	245.6	349.4	442.2
Average Forces on Z axis [N]	105.4	136.8	196.4	248.1	297.6

Experiments were implemented on Aluminum 7050-T7451 and the workpiece and its computer aided design (CAD) model are shown in Figure 3.10.

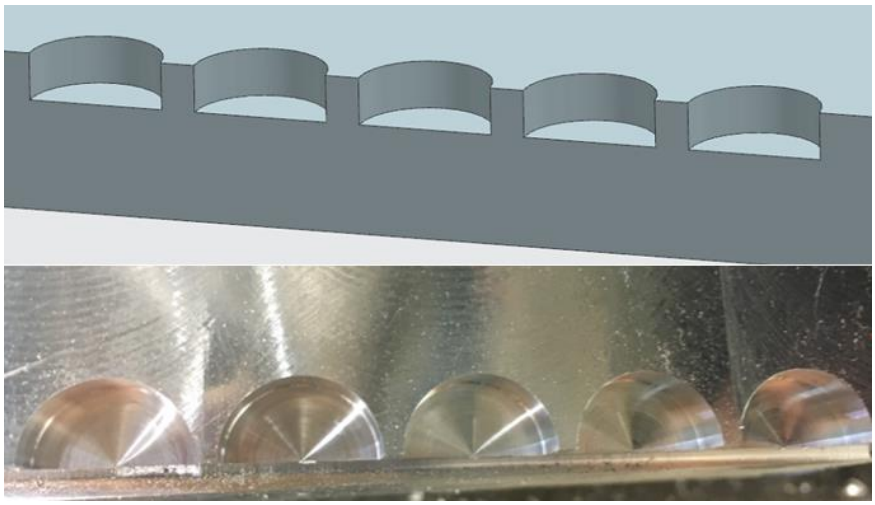

Figure 3.10 Half plunge milling workpiece (bottom), CAD model of the workpiece (top)

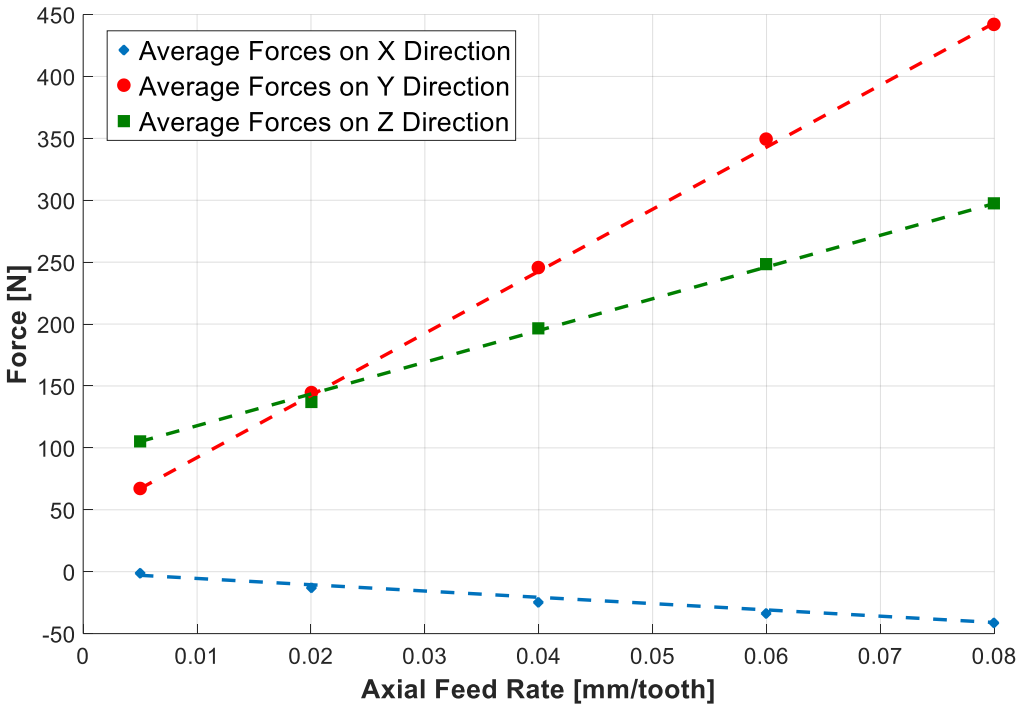

Figure 3.11 Average forces on each axis for half plunge milling

The average forces are fitted to a line (Equation. 3.14) with a linear least squares, and the estimated cutting force coefficients are given in Table 3.2

Table 3.2 Identified cutting force coefficients for the bottom part of the tool and

$K_{rc,b}$ [MPa]	$K_{re,b}$[N/mm]	$K_{tc,b}$[MPa]	$K_{te,b}$[N/mm]	$K_{ac,b}$[MPa]	$K_{ae,b}$[N/mm]
104.63	0.20	986.04	8.62	326.44	11.22

3.4 Prediction of Cutting Forces

The spindle speed n and orbital travel speed n_o are given in [rev/min] with corresponding angular speeds in [rad/s]:

$$\omega = \frac{2\pi n}{60}, \Omega = \frac{2\pi n_o}{60} \tag{3.15}$$

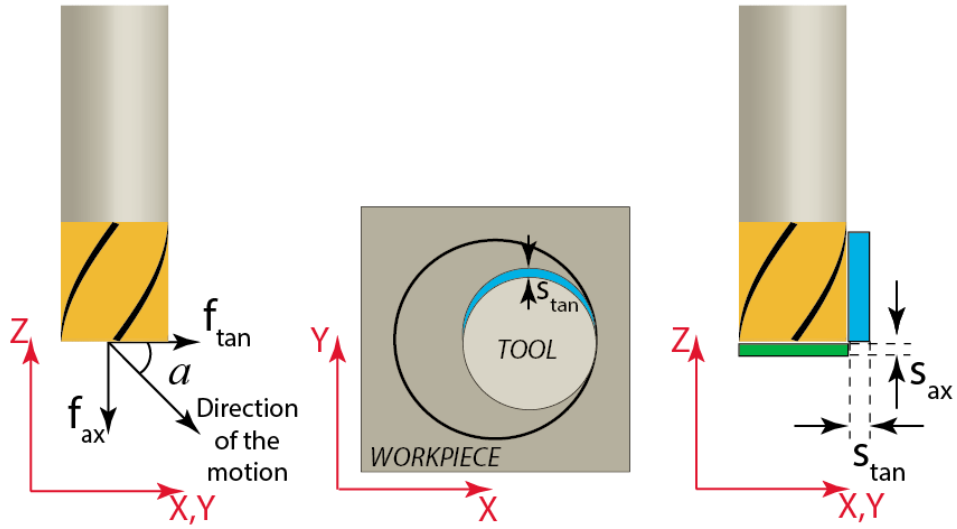

Figure 3.12 Tangential and axial feed directions

Tangential linear feed (f_{tan}) and feed rate (s_{tan}) are evaluated in feed direction (x_c) from Figure 3.12.

$$f_{\tan} = \Omega\left(\frac{D_H - D_T}{2}\right)$$
$$s_{\tan} = f_{\tan}\frac{60}{Nn} \tag{3.16}$$

The axial feed f_{ax} and feed rate s_{ax} along the axial (Z) direction are evaluated by considering the ramp angle of the tool path α (Figure 3.12):

$$\alpha = \tan^{-1}\left(\frac{\pi D_P}{a_p}\right) \leftarrow D_P = D_H - D_T \tag{3.17}$$

Where D_P is the diameter of the tool path. The axial linear feed (f_{ax}) and the axial feed rate per tooth s_{ax} are given by:

$$f_{ax} = f_{\tan} \tan\alpha = \Omega\left(\frac{D_H - D_T}{2}\right)\tan\alpha$$
$$s_{ax} = s_{\tan} \tan\alpha = f_{\tan}\frac{60}{Nn}\tan\alpha \tag{3.18}$$

The instantaneous immersion angle of a tooth j at elevation z can be evaluated :

$$\phi_{j,r}(k) = \phi_{j0,r} + (\mathrm{j}-1)\phi_{pitch} + z\frac{\tan\beta_h}{R_T} \tag{3.19}$$

where $\emptyset_{j0,r}$ is the immersion angle of the associated cutting flute at the bottom and β_h is the helix angle of the cylindrical end mill with N number of flutes. The chip thickness within the engagement zone is defined by:

$$h_j = g\left(\phi_{j,r}(k)\right)\cdot s_{\tan}\sin\phi_{j,r}(k) \tag{4.20}$$

Where the following unit pulse function indicates whether the flute is in or out of material:

$$g\left(\phi_{j,r}(k)\right) = \begin{cases} 1 & if\ \ \phi_{st,r}(z) \le \phi_{j,r}(k) \le \phi_{ex,r} \\ 0 & else \end{cases} \tag{3.21}$$

The cutting forces contributed by a cutting edge segment with a differential height (*dz*) are evaluated from Figure 3.13 as:

$$dF_{tj,\mathrm{r}} = K_{tc,r}h_j dz + K_{te,r}dz$$
$$dF_{rj,\mathrm{r}} = K_{rc,r}h_j dz + K_{re,r}dz \tag{3.22}$$
$$dF_{aj,\mathrm{r}} = K_{ac,r}h_j dz + K_{ae,r}dz$$

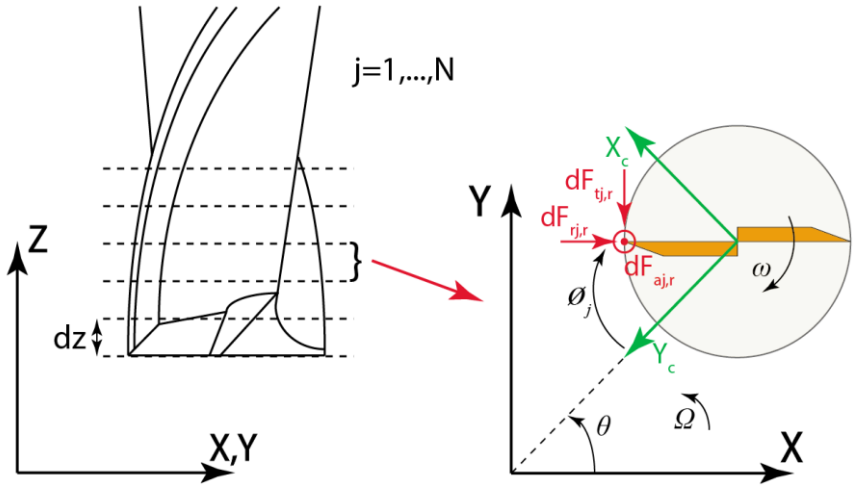

Figure 3.13 Radial, tangential and axial cutting forces on the radial part of the tool at one discrete element

The total forces generated by the peripheral edges of the end mill can be calculated by summing the projected differential forces in the cartesian axes as:

$$F_{x,r}(\theta,\phi)=\sum_{j=1}^{N} g(\phi_{j,r})\Big[(-F_{\mathrm{tj},r}\cos\phi_j - F_{\mathrm{rj},r}\sin\phi_j)\sin\theta+(F_{\mathrm{tj},r}\sin\phi_j - F_{\mathrm{rj},r}\cos\phi_j)\cos\theta\Big]$$

$$F_{\mathrm{y},r}(\theta,\phi)=\sum_{j=1}^{N} g(\phi_{j,r})\Big[-(-F_{\mathrm{tj},r}\cos\phi_j - F_{\mathrm{rj},r}\sin\phi_j)\cos\theta+(F_{\mathrm{tj},r}\sin\phi_j - F_{\mathrm{rj},r}\cos\phi_j)\sin\theta\Big] \quad (3.23)$$

$$F_{\mathrm{z},r}(\theta,\phi)=\sum_{j=1}^{N} g(\phi_{j,r})\Big[F_{\mathrm{aj},r}\Big]$$

The cutting forces contributed by the bottom edges of the end mill are evaluated when the tool plunges in the workpiece as:

$$F_{x,\mathrm{b}}(\theta,\phi)=\sum_{j=1}^{N}\Big[(-F_{\mathrm{tj,b}}\cos\phi_j - F_{\mathrm{rj,b}}\sin\phi_j)\sin\theta+(F_{\mathrm{tj,b}}\sin\phi_j - F_{\mathrm{rj,b}}\cos\phi_j)\cos\theta\Big]$$

$$F_{\mathrm{y,b}}(\theta,\phi)=\sum_{j=1}^{N}\Big[-(-F_{\mathrm{tj,b}}\cos\phi_j - F_{\mathrm{rj,b}}\sin\phi_j)\cos\theta+(F_{\mathrm{tj,b}}\sin\phi_j - F_{\mathrm{rj,b}}\cos\phi_j)\sin\theta\Big] \quad (3.24)$$

$$F_{\mathrm{z,b}}(\theta,\phi)=\sum_{j=1}^{N}\Big[F_{\mathrm{aj,b}}\Big]$$

The total forces contributed by the peripheral and bottom edges of the tool are:

$$\begin{aligned} F_{\mathrm{x},Total} &= F_{x,r} + F_{x,\mathrm{b}} \\ F_{y,Total} &= F_{y,\mathrm{r}} + F_{y,\mathrm{b}} \\ F_{z,Total} &= F_{\mathrm{z},r} + F_{z,\mathrm{b}} \end{aligned} \tag{3.25}$$

3.5 Simulations and Experimental Results

Series of orbital drilling tests have been carried out on Quaser UX600 5 axis machining center instrumented with a Kistler 9255B table top dynamometer as shown in Figure 3.14.

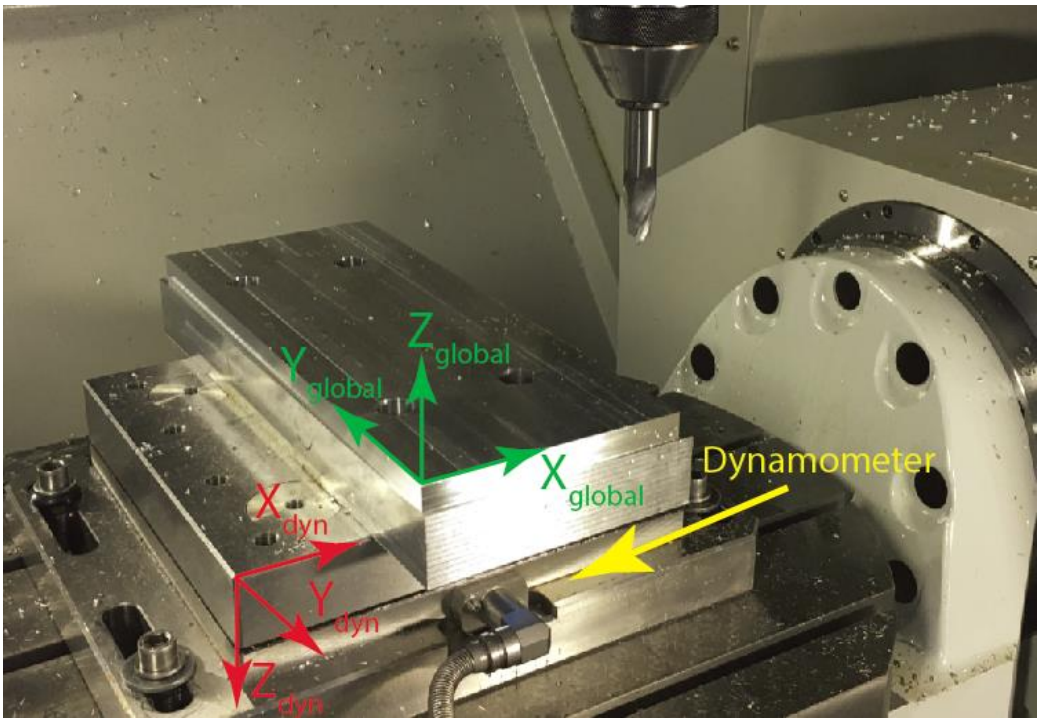

Figure 3.14 Experimental setup for mechanics test

The geometric properties of the helical end mill used in orbital drilling tests are shown in Table 3.3 and the cutting conditions are given in Table 3.4.

Table 3.3 Specifications of the carbide end mill used for the experiments

Tool Type	Cutting Diameter	Radial Rake Angle	Axial Rake Angle	Flute Helix Angle	Max. Ramping Angle	Orbital Drilling Capability
2- Fluted Solid Flat-End mill	16 mm	13.5°	13.5°	25°	15°	Yes

3 experiments with different process parameters are experimentally verified and the parameters of each experiment are listed as follows.

Table 3.4 Cutting conditions used in orbital drilling tests.

Exp #	Hole Diameter [mm]	Spindle Speed [RPM]	Orbital Speed [RPM]	Pitch Length of the Tool Path [mm]	Tangential Feed Rate [mm/rev/tooth]	Axial Feed Rate [mm/rev/tooth]
1	25	1000	10	3	0.1414	0.015
2	25	1000	10	6	0.1414	0.030
3	30	1000	5	4.5	0.11	0.0113

The workpiece material was selected Aluminum 7050-T7451 with the cutting force coefficients $K_{tc,r}$ = 884.65 [MPa], $K_{te,r}$ = 15.33 [N/mm], $K_{rc,r}$ = 214.64 [MPa], $K_{re,r}$ = 35.36 [N/mm], $K_{ac,r}$ = 185.14 [MPa], $K_{ac,r}$ = 0 [N/mm]. Cutting coefficients related with the bottom part of the tool was given on the Table 3.2. When the cutting coefficients on both sides of the end mill are compared, the difference for both cutting and edge coefficients of radial, tangential and axial directions is obvious. The reason behind this difference is the cutting geometry on the periphery and on the axial part of the tool which are different. In addition to that, for

mechanistically calibrating the cutting force coefficients on the bottom part of the tool, cutting force coefficients are assumed to be constant throughout the cutter radius. However since the cutting speed is changing throughout the radius of the end mill, the cutting force coefficient values shouldn't be different considering the orthogonal to oblique transformation approach. In order to present a more realistic solution the bottom geometry should be analyzed with an advanced tool microscope. The simulated maximum radial engagement conditions for each experimental case are shown in Figure 3.15.

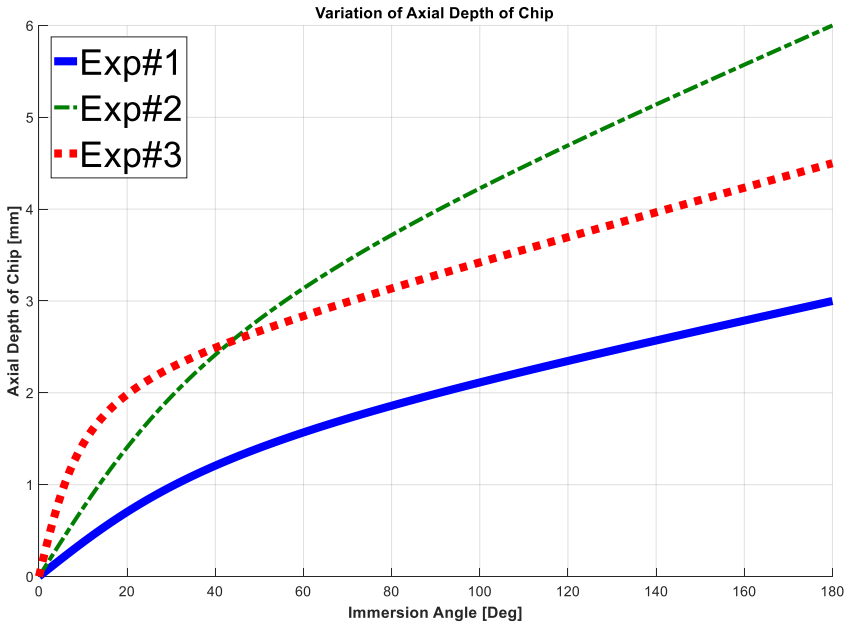

Figure 3.15 Simulated maximum radial engagement boundaries for experiments

The predicted and experimentally measured cutting forces of experiment 1 in zone 2 of orbital drilling operation are given for one travel period of tool around the hole center in Figure 3.16 and Figure 3.17 respectively. Simulated and experimental results consider the cutting forces when tool starts cutting in zone 2 and rotates around the hole center 360 degrees which is equal to the pitch length of the path in vertical direction. A detailed comparison of the predicted and measured forces is given in Figure 3.18.

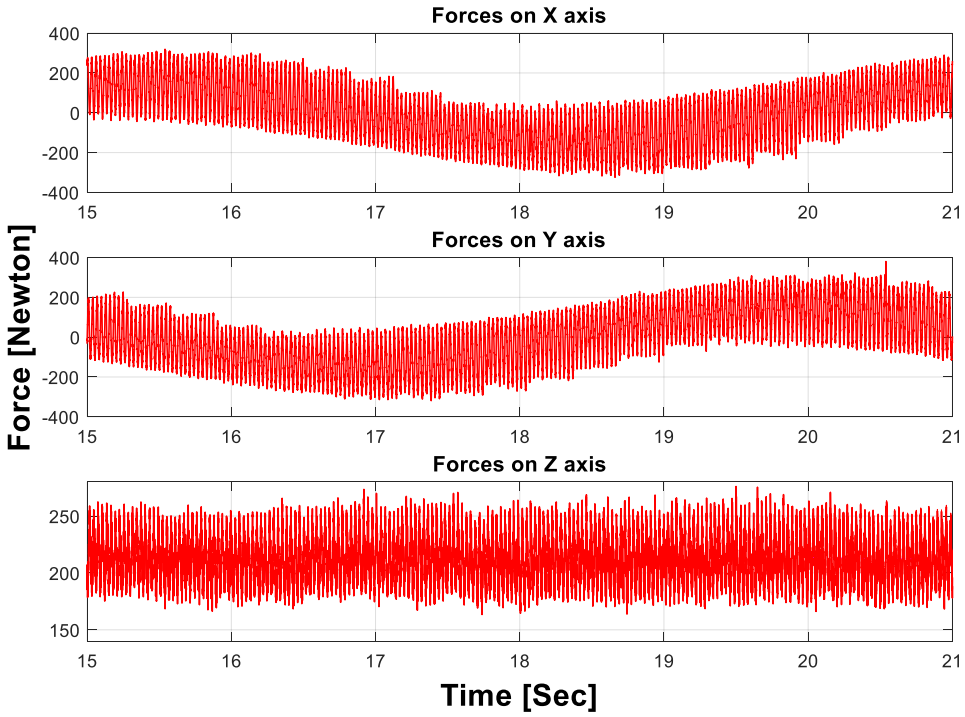

Figure 3.16 Measured cutting forces in x, y and z directions (Exp#1)

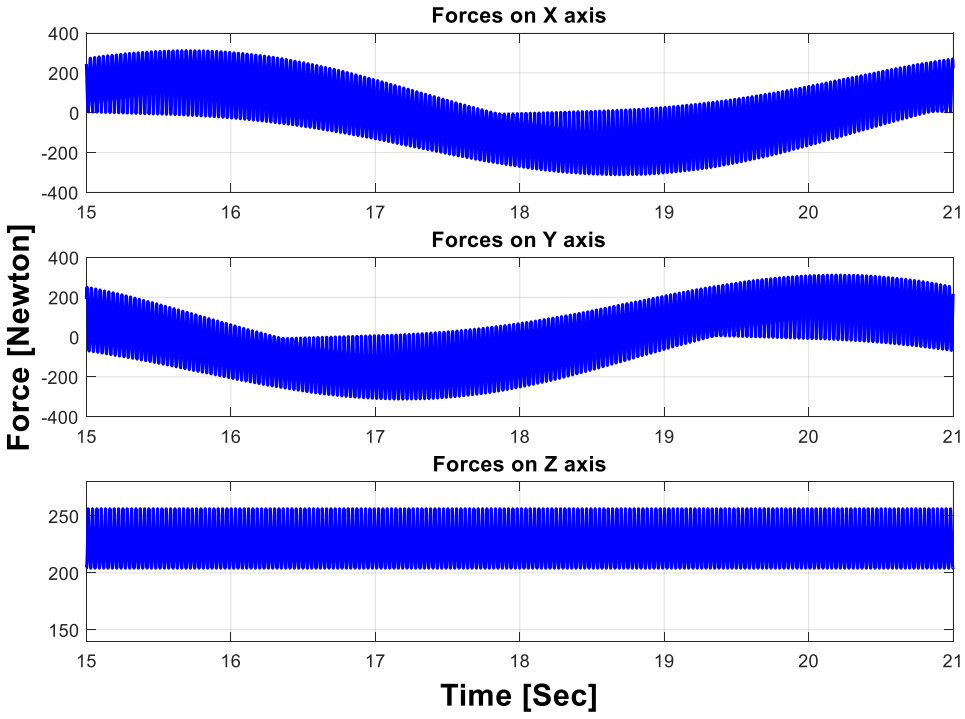

Figure 3.17 Predicted cutting forces in x, y and z directions (Exp#1)

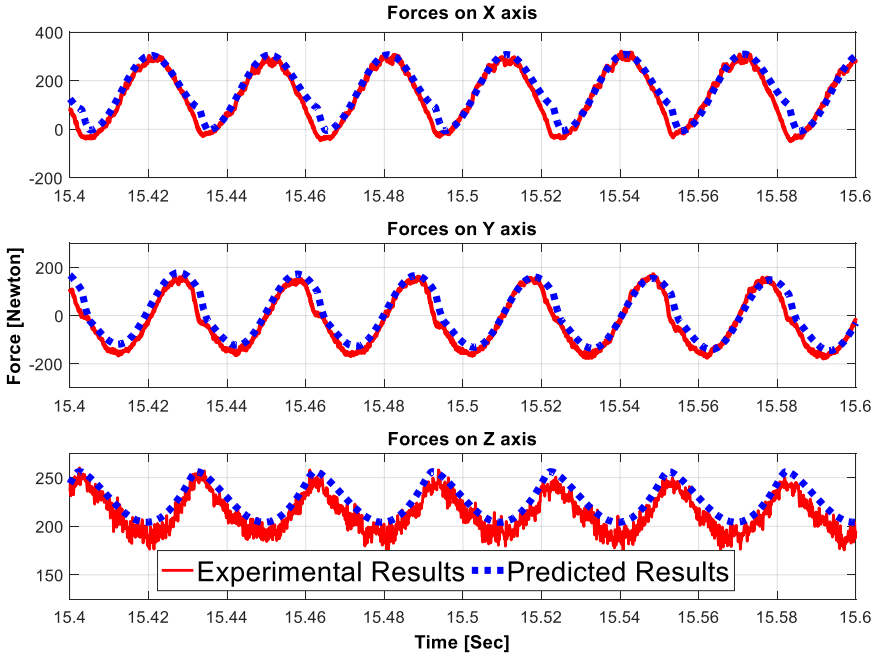

Figure 3.18 Comparison of measured and predicted cutting forces (Exp#1)

The predicted and measured forces for the experiments 2 and 3 are shown in Figure 3.19 and Figure 3.20, respectively.

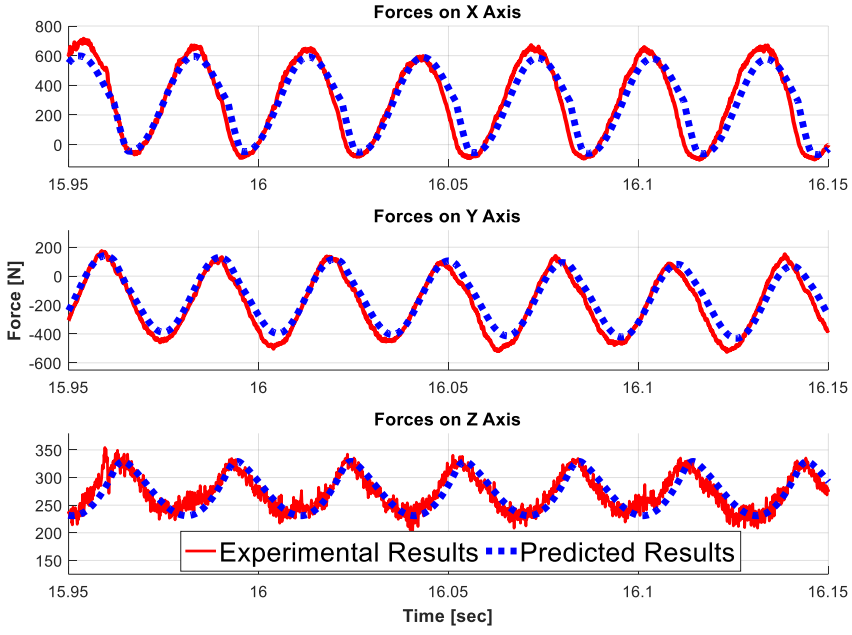

Figure 3.19 Comparison of measured and predicted cutting forces (Exp#2)

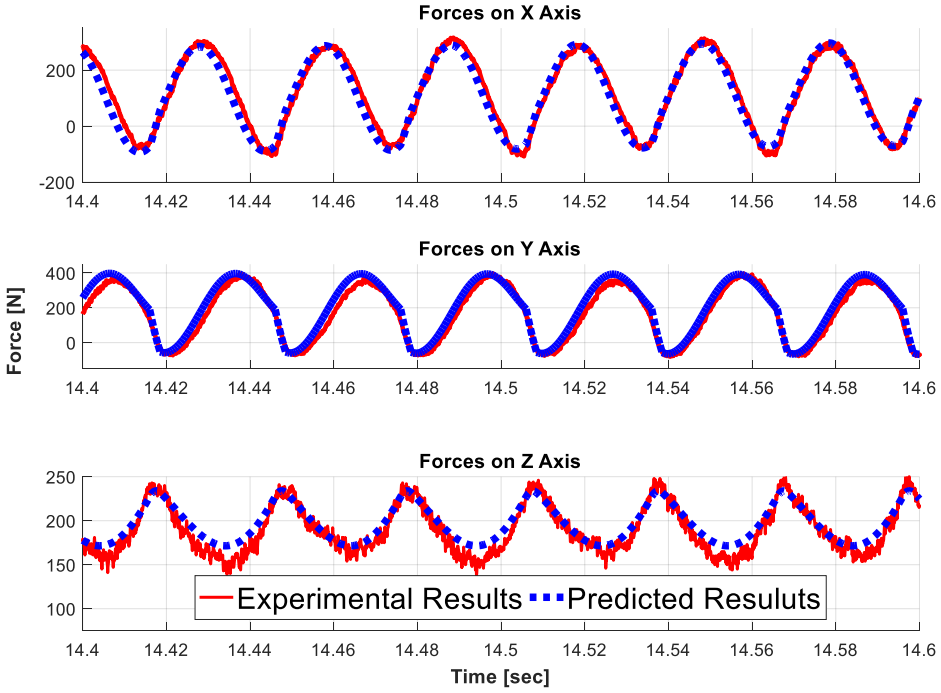

Figure 3.20 Comparison of measured and predicted cutting forces (Exp#3)

While the prediction accuracy is quite satisfactory in radial (X, Y) directions, there are slight deviations in the axial (Z) direction due to uncertainties in modeling the plunge cutting process. The prediction errors are shown on average axial forces in Table 3.5.

Table 3.5 Prediction errors on average axial forces.

	Average Predicted Force [N]	**Average Measured Force [N]**	**Average Error (%)**
Experiment #1	229	211	8.5
Experiment #2	281	273	2.9
Experiment #3	196	204	3.9

Chapter 4: Chatter Stability of Orbital Drilling Operations

4.1 Introduction

Chatter is a self-excited vibration that is caused by the phase shift between two successive waves left on the workpiece material during the metal cutting operations. Chatter must be avoided to obtain good surface finish and high material removal rates while avoiding tool breakage and high dynamic loads on machine tool spindle.

The acceptable quality of machined surface is determined by the static and dynamic deflections of the flexible tool which are imprinted on the hole surface. The mechanics of orbital drilling which leads to prediction of chip thickness and forces are presented in the previous chapter. This chapter extends the model to include the effects of vibrations on the chip thickness hence on the dynamic forces. The dynamic model allows the identification of chatter stability diagrams which lead to stable speeds and cutting engagement conditions which yield to good surface finish and high material removal rate. The model also allows the prediction of static deflection and forced vibration marks left on the hole surface.

Henceforth, the chapter is organized as follows. First, the dynamic model of orbital drilling is modeled and the effect of orbital motion on time delay investigated. The chatter stability of the orbital drilling is solved both in frequency and semi-discrete time domain. The varying engagement conditions and position dependent structural dynamics of the tool are considered in the stability models. The models are experimentally verified.

4.2 Dynamic Cutting Forces in Orbital Drilling

Dynamic cutting forces excite the machine tool structure in both radial (x,y) and axial (z) directions in global coordinate system. The dynamic displacements in the tangential and axial chip thicknesses are derived in terms of tools instantaneous angular position around hole (θ), instantaneous immersion angle at both radial and bottom part of the end mill $\emptyset_j$, and vibrations in global coordinates Δx, Δy, Δz as follows:

$$\begin{gathered} h_r\left(\phi_j,\theta\right)=s_{\tan}\sin\left(\phi_{j,r}\right)-\Delta x\cos\left(\phi_{j,r}-\theta\right)+\Delta y\sin\left(\phi_{j,r}-\theta\right) \\ h_{ax}\left(\phi_j,\theta\right)=s_{ax}+\Delta z \\ \textit{where} \\ h_r\left(\phi_{j,r}\right)=s_{\tan}\sin\left(\phi_{j,r}\right)+\Delta x_c\left(t\right)\sin\left(\phi_{j,r}\right)+\Delta y_c\left(t\right)\cos\left(\phi_{j,r}\right) \\ \Delta x_c\left(t\right)=-\Delta x\left(t\right)\sin\left(\theta\right)+\Delta y\left(t\right)\cos\left(\theta\right) \\ \Delta y_c\left(t\right)=-\Delta x\left(t\right)\cos\left(\theta\right)-\Delta y\left(t\right)\sin\left(\theta\right) \\ \Delta z_c\left(t\right)=\Delta z\left(t\right) \end{gathered} \tag{4.1}$$

$s_{\tan}\sin\left(\phi_{j,r}\right)$ is the static and $-\Delta x\cos\left(\phi_{j,r}-\theta\right)+\Delta y\sin\left(\phi_{j,r}-\theta\right)$ represents the dynamic part of the chip thickness in global coordinates. $\Delta x\left(t\right)=x(t)-x(t-\tau)$, $\Delta y\left(t\right)=y(t)-y(t-\tau)$ and $\Delta z\left(t\right)=z(t)-z(t-\tau)$ denotes the difference between dynamic displacements at present and previous cuts in global coordinates. The static chip thickness does not affect the chatter stability when the cutting force coefficient is constant, hence it can be dropped from the stability formulation [32]. The tangential and axial chip thicknesses can be rewritten as follows:

$$\begin{gathered} h_r\left(\phi_j,\theta\right)=-\Delta x\cos\left(\phi_{j,r}-\theta\right)+\Delta y\sin\left(\phi_{j,r}-\theta\right) \\ h_{ax}\left(\phi_j,\theta\right)=\Delta z \end{gathered} \tag{4.2}$$

The cutting forces are evaluated in global coordinates

$$\begin{aligned} F_{x,r}\left(\phi_j,\theta\right) &= K_{tc,r}a\left(\phi_j\right)h_r\left(\phi_j,\theta\right)\left(\sin\left(\phi_j-\theta\right)\right)-K_{rc,r}a\left(\phi_j\right)h_r\left(\phi_j,\theta\right)\left(\cos\left(\phi_j-\theta\right)\right) \\ F_{\mathrm{y},r}\left(\phi_j,\theta\right) &= K_{tc,r}a\left(\phi_j\right)h_r\left(\phi_j,\theta\right)\left(\cos\left(\phi_j-\theta\right)\right)+K_{rc,r}a\left(\phi_j\right)h_r\left(\phi_j,\theta\right)\left(\sin\left(\phi_j-\theta\right)\right) \\ F_{\mathrm{z},r}\left(\phi_j,\theta\right) &= K_{ac,r}a\left(\phi_j\right)h_r\left(\phi_j,\theta\right) \end{aligned} \quad (4.3)$$

Where $K_{tc,r}$, $K_{rc,r}$, $K_{ac,r}$, are cutting force coefficients, $\emptyset_j$ instantaneous immersion angle of tooth j, $a(\emptyset_j)$ is the instantaneous depth of cut, and $h_r(\emptyset_j,\theta)$ is radial chip thickness. Dynamic cutting forces at the bottom part of the end mill acting on tooth j is expressed

$$\begin{aligned} F_{x,\mathrm{b}}\left(\phi_j,\theta\right) &= K_{tc,\mathrm{b}}R_T h_{ax}\left(\phi_j,\theta\right)\left(\sin\left(\phi_j-\theta\right)\right)-K_{rc,\mathrm{b}}R_T h_{ax}\left(\phi_j,\theta\right)\left(\cos\left(\phi_j-\theta\right)\right) \\ F_{\mathrm{y,b}}\left(\phi_j,\theta\right) &= K_{tc,\mathrm{b}}R_T h_{ax}\left(\phi_j,\theta\right)\left(\cos\left(\phi_j-\theta\right)\right)+K_{rc,\mathrm{b}}R_T h_{ax}\left(\phi_j,\theta\right)\left(\sin\left(\phi_j-\theta\right)\right) \\ F_{\mathrm{z,b}}\left(\phi_j,\theta\right) &= K_{ac,\mathrm{b}}R_T h_{ax}\left(\phi_j,\theta\right) \end{aligned} \quad (4.4)$$

Where $K_{tc,b}$, $K_{rc,b}$, $K_{ac,b}$ are the cutting coefficients for the bottom part of the cuing edges, $h_{ax}(\emptyset_j,\theta)$ is the axial chip thickness.

By considering the contributions of both radial and bottom part of the end mill, dynamic forces acting on tooth j can be as:

$$\begin{Bmatrix} F_{xj} \\ F_{\mathrm{yj}} \\ F_{\mathrm{zj}} \end{Bmatrix} = \frac{1}{2} a\left(\phi_j\right) \begin{bmatrix} \left(K_{tc,r}\sin\left(2A\right)+K_{rc,r}\left(1+\cos\left(2A\right)\right)\right) & \left(K_{tc,r}\left(1-\cos\left(2A\right)\right)-K_{rc,r}\sin\left(2A\right)\right) & \frac{2R_T}{a\left(\phi_j\right)}\left(K_{tc,\mathrm{b}}\sin\left(A\right)-K_{rc,\mathrm{b}}\cos\left(A\right)\right) \\ \left(K_{tc,r}\left(-1-\cos\left(2A\right)\right)-K_{rc,r}\sin\left(2A\right)\right) & \left(K_{tc,r}\sin\left(2A\right)+K_{rc,r}\left(1+\cos\left(2A\right)\right)\right) & \frac{2R_T}{a\left(\phi_j\right)}\left(K_{tc,\mathrm{b}}\cos\left(A\right)+K_{rc,\mathrm{b}}\sin\left(A\right)\right) \\ \left(-2K_{ac,r}\cos\left(A\right)\right) & \left(2K_{ac,r}\sin\left(A\right)\right) & \frac{2R_T}{a\left(\phi_j\right)}\left(K_{ac,\mathrm{b}}\right) \end{bmatrix} \begin{Bmatrix} \Delta x\left(t\right) \\ \Delta y\left(t\right) \\ \Delta z\left(t\right) \end{Bmatrix} \tag{4.5}$$

Where

$$A = \phi_j - \theta \tag{4.6}$$

Total dynamic cutting forces F_x, F_y and F_z can be evaluated by summing the forces contributed by all the teeth which are engaged with the workpiece:

$$\begin{aligned} F_{x\left(\phi_j,\theta\right)} &= \sum_{j=1}^{N} F_{xj} \\ F_{y\left(\phi_j,\theta\right)} &= \sum_{j=1}^{N} F_{yj} \\ F_{z\left(\phi_j,\theta\right)} &= \sum_{j=1}^{N} F_{zj} \end{aligned} \tag{4.7}$$

4.3 Chatter Stability in Orbital Drilling

The chatter stability of orbital drilling process is solved in frequency domain and semi-discrete time domain with the following assumptions:

- The radial chip load is always greater than the axial chip load due to the helical-orbital motion of the tool. Hence, it is assumed that the main source of the chatter is by the lateral deflections of the end mill and axial deflections are neglected in the chatter stability solution.
- Since the core of the end mills are stronger than twist drills the torsional modes of the end mill is neglected.
- Gyroscopic effects that might come from the orbital motion of the cutter are negligible due to slow orbital motion.

Since the feed direction changes during the orbital motion, FRF of the machine on global coordinates is oriented onto the local coordinates of the end mill in lateral directions. As a result, the stability model is 3D and dependent on the position of the tool, spindle speed and axial pitch length of the tool path. Different than the approach presented by Li et al. [16], in frequency domain solution the exact engagement conditions are taken into account for solving the chatter stability of the operation. Besides, the presented semi-discrete time domain solution is the first attempt to study the dynamics of orbital drilling in time domain.

4.3.1 Orbital Motion Effect on Time Delay

The stability of machining processes with by two different delay terms contributed by the spindle speed and feed motions has been studied before [17, 18]. Here, the effect of tool's orbital helical motion on the regenerative delay is studied using an analysis model proposed by Long et al [33]. The spindle speed n and orbital speed n_o are expressed in [rad/sec] as:

$$\omega[rad/sec]=\frac{2\pi n}{60},\quad \Omega[rad/sec]=\frac{2\pi n_o}{60} \tag{4.8}$$

Which leads to tangential feed f_{tan}[mm/sec] :

$$f_{\tan}=\Omega\left(\frac{D_H-D_T}{2}\right) \tag{4.9}$$

The motion of the end mill's tooth after one tooth period is shown in Figure 4.1 where end mill's center shifts from (O_1) to (O_2). The dashed and solid lines represent the tool paths of the first and the second tooth, respectively. O_1 is the position of tool center when the first tooth cuts the workpiece at point B and O_2 is the position of tool center when the subsequent tooth cuts the workpiece at point A. The kinematics of the motion leads to static chip thickness $\overline{AB}$.

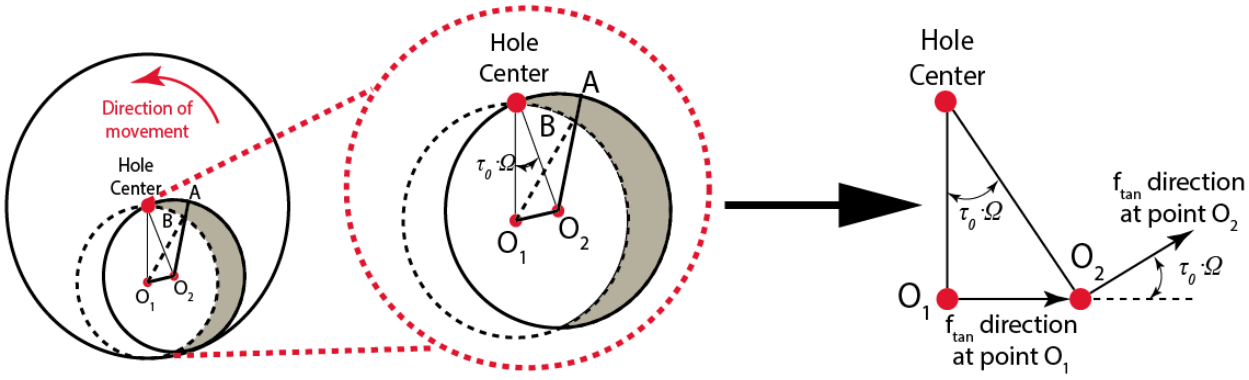

Figure 4.1 Toolpath of orbital drilling process and simultaneous feed directions

In practice, the orbital speed (n_o) is significantly lower than the spindle speed (n), i.e. $\frac{n}{n_o} \geq 100$. The speed ratio could change as a function of tool diameter, hole diameter and cutting conditions such as tangential and axial feed rates. Hence the angular orientation of the feed in one tooth period ($\tau_0 = \frac{60}{Nn}$) ($\tau_0 \cdot \Omega$) between two consecutive tool centers is extremely small:

$$\delta = \tau_0 \Omega = \frac{60}{Nn} \frac{2\pi n_0}{60} = \frac{2\pi}{N} \frac{n_0}{n} \tag{4.10}$$

For a two fluted end mill ($N = 2$), orbital speed $n_0 = 12\,[rev/\min]$ and spindle speed of $n = 1200\,[rev/\min]$, the angular change in the direction of feed is 0.0314[rad] or 1.8 degrees which is negligible. As a result, it is assumed that the structural dynamics of the system in one tooth period are assumed to remain constant.

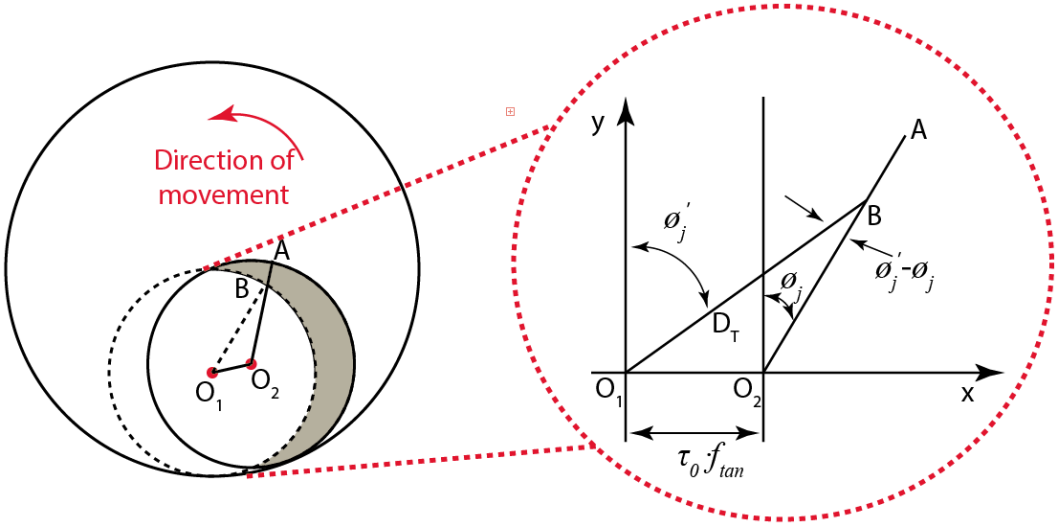

Figure 4.2 Vibration independent toolpath of orbital drilling process

If the $\emptyset'_j$ and $\emptyset_j$ are assumed to be equal the constant time delay (tooth period) can be evaluated as:

$$\tau_0 = \frac{60}{Nn} \tag{4.11}$$

If the vibrations of the tool are neglected, tool center shifts at amount of:

$$\overline{O_1 O_2} \approx \tau_0 f_{\tan} \tag{4.12}$$

By using the sine rule:

$$\frac{\tau_0 f_{\tan}}{\sin\left(\phi'_j - \phi_j\right)} = \frac{D_T / 2}{\sin\left(\pi / 2 + \phi_j\right)} = \frac{D_T / 2 - \overline{AB}}{\cos\left(\phi'_j\right)} \tag{4.13}$$

In practical orbital drilling applications $\tau_0 f_{\tan}$ is much smaller than the radius of the cutter hence the following assumption is made:

$$\sin\left(\phi'_j - \phi_j\right) \approx \phi'_j - \phi_j \tag{4.14}$$

By using the definition of time delay:

$$\tau = \tau_0 - t' = \frac{2\pi / N}{\omega} - \frac{\left(\phi'_j - \phi_j\right)}{\omega} = \tau_0 - \frac{\left(\phi'_j - \phi_j\right)}{\omega} \leftarrow \omega = \frac{2\pi n}{60} \tag{4.15}$$

Where *t'* is the time at which the previous cutter tooth reaches at the angular position $\emptyset'_j$ and *t* is the time when the current cutter tooth reaches at the angular position $\emptyset_j$.

Varying time delay is derived as:

$$\tau\left(\phi_j\right)=\frac{\pi D_T}{N\left(\omega D_T/2+f_{\tan}\cos\phi_j\right)}=\frac{\pi D_T}{N\left(\omega D_T/2+\left(\Omega\left(\frac{D_H-D_T}{2}\right)\right)\cos\phi_j\right)} \quad (4.16)$$

As it can be seen from the Equation 4.16 the effect of orbital motion on time delay depends on the hole diameter D_H, tool diameter D_T, spindle speed ω [rad/sec] and orbital speed Ω [rad/sec].

Time delays are evaluated as a function of orbital speeds, with fixed tool and hole diameters at the angular position of the each tooth in Figure 4.3. The following parameters are used in the analysis: spindle speed n = 8000 rpm, tool diameter D_T = 16 mm, hole diameter D_H = 30 mm, number of the teeth N = 2. The following orbital speeds and tangential feed rates are used:

i. n_o = 20 rpm, $s_{\tan}$ = 0.055 mm/tooth/rev

ii. n_o = 40 rpm, $s_{\tan}$ = 0.110 mm/tooth/rev

iii. n_o = 80 rpm, $s_{\tan}$ = 0.220 mm/tooth/rev

iv. n_o = 120 rpm, $s_{\tan}$ = 0.330 mm/tooth/rev

In practical orbital drilling operations, the tangential feed rate (s_{tan}) is often less than 0.25 mm/tooth/rev. As the orbital speed increases, the variable delay changes. For the case where the orbital speed is n_o = 120 rpm, the variation in the delay amplitude is expected to be less than 1.5% of constant time delay (τ_0).

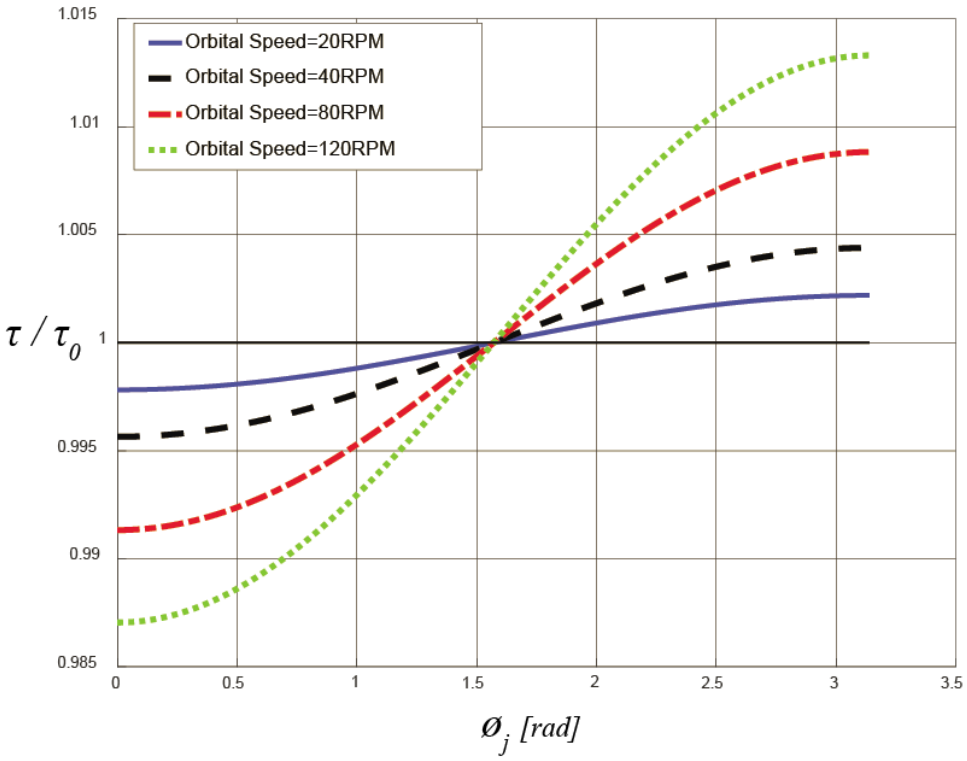

Figure 4.3 Variable time delay versus angular position of cutting tooth

The results given in Figure 4.3 demonstrates the real time delay remains within ±1.5% of the tooth period at extreme orbital speeds, hence the effect of orbital speed on the delay term used in chatter stability is negligible.

4.3.2 Chatter Stability in Frequency Domain Solution

If the cutting with the bottom part is neglected the dynamics of the orbital drilling at a frozen point along the path is similar to the milling. The regeneration of radial chip thickness is shown in Figure 4.4 and can be expressed as [32]:

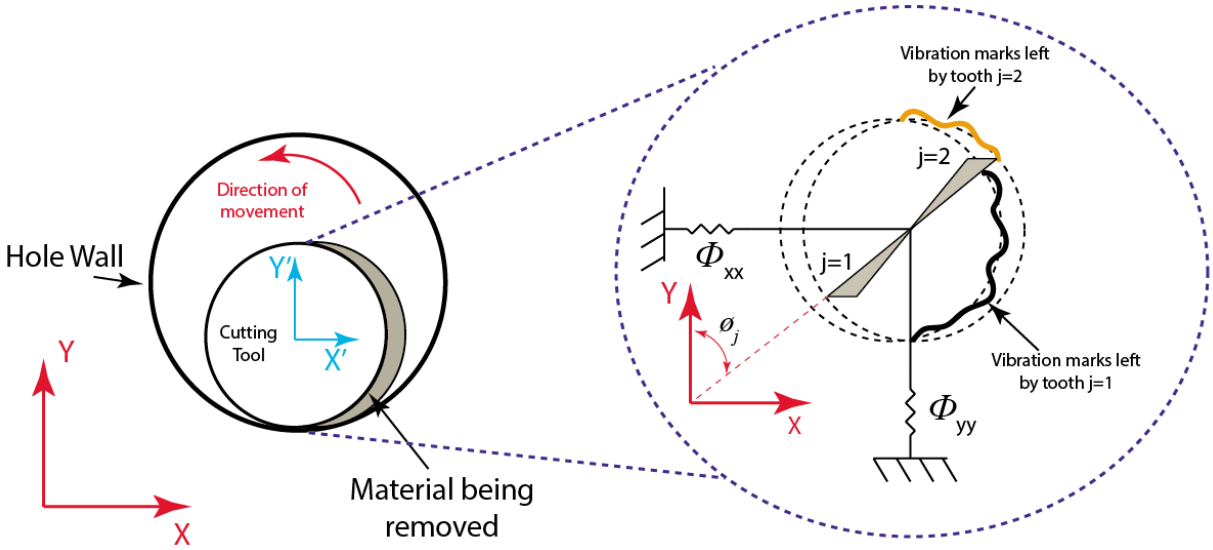

Figure 4.4 Dynamic radial chip thickness generation in orbital drilling

$$h_r\left(\phi_{j,r}\right)=\Delta x\sin\left(\phi_{j,r}\right)+\Delta y\cos\left(\phi_{j,r}\right) \tag{4.17}$$

The dynamic cutting forces in x and y directions are:

$$\begin{Bmatrix}F_x\\F_y\end{Bmatrix}=\frac{1}{2}aK_{tc,r}\begin{bmatrix}a_{xx}&a_{xy}\\a_{yx}&a_{yy}\end{bmatrix}\begin{Bmatrix}\Delta x\\\Delta y\end{Bmatrix} \tag{4.18}$$

where the time varying directional dynamic milling coefficients are represented by

$$\begin{aligned} a_{xx} &= -\sum_{j=0}^{N-1}\left[\sin 2\phi + K_{r,r}\left(1-\cos 2\phi\right)\right] \\ a_{xy} &= -\sum_{j=0}^{N-1}\left[\left(1+\cos 2\phi\right) + K_{r,r}\sin 2\phi\right] \\ a_{yx} &= \sum_{j=0}^{N-1}\left[\left(1-\cos 2\phi\right) - K_{r,r}\sin 2\phi\right] \\ a_{yy} &= \sum_{j=0}^{N-1}\left[\sin 2\phi - K_{r,r}\left(1+\cos 2\phi\right)\right] \end{aligned} \tag{4.19}$$

$K_{r,r} = K_{rc,r} / K_{\mathrm{tc},r}$. The dynamic cutting forces in time domain can be expressed in vector form as:

$$\left\{F(t)\right\} = \frac{1}{2} K_{tc,r} a\left[D(t)\right]\left\{\Delta(t)\right\} \tag{4.20}$$

Where $D(t)$ is the time varying directional matrix. Altintas and Budak [27] introduced frequency domain linear stability law to predict critically stable depth of cut and spindle speeds as a function of machine's dynamics, tool geometry and work material properties. They transformed the time varying, periodic directional matrix into frequency domain:

$$\begin{aligned} \left[D(t)\right] &= \sum_{r=-\infty}^{\infty}\left[D_r\right]e^{ir\omega_\tau t} \\ \left[D_r\right] &= \frac{1}{\tau}\int_0^\tau \left[D(t)\right]e^{ir\omega_\tau t}dt \end{aligned} \tag{4.21}$$

Where τ is the tooth passing period. Budak and Altintas [34] proposed two approaches: Multi-Frequency solution where the harmonics of periodic coefficients are considered; and Zero Order method where the harmonics are neglected to eliminate time dependency of directional

coefficient. The Zero Order method is used here by taking only the mean value of directional coefficients as:

$$[D_0] = \frac{1}{\tau}\int_0^{\tau} [D(t)]dt \tag{4.22}$$

Which is valid only when the tool is in engagement boundaries ($\phi_{st,r}$, $\phi_{ex,r}$)

$$[D_0] = \frac{1}{\phi_{pitch}}\int_{\phi_{st,r}}^{\phi_{ex,r}} [D(\phi)]d\phi \tag{4.23}$$

Where ϕ_{pitch} is the pitch angle of the cutter. The resulting average directional milling coefficients become:

$$\begin{aligned}
a_{xx} &= \frac{1}{2}\left[\cos 2\phi - 2K_{r,r}\phi + K_{r,r}\sin 2\phi\right]_{\phi_{st,r}}^{\phi_{ex,r}} \\
a_{xy} &= \frac{1}{2}\left[-\sin 2\phi - 2\phi + K_{r,r}\cos 2\phi\right]_{\phi_{st,r}}^{\phi_{ex,r}} \\
a_{yx} &= \frac{1}{2}\left[-\sin 2\phi + 2\phi + K_{r,r}\cos 2\phi\right]_{\phi_{st,r}}^{\phi_{ex,r}} \\
a_{yy} &= \frac{1}{2}\left[-\cos 2\phi - 2K_{r,r}\phi - K_{r,r}\sin 2\phi\right]_{\phi_{st,r}}^{\phi_{ex,r}}
\end{aligned} \tag{4.24}$$

The dynamic cutting forces in Equation 4.20 can be expressed as:

$$\{F(i\omega)\} = \frac{1}{2}K_{tc,r}a[D_0]\{\Delta(i\omega)\} \tag{4.25}$$

The lateral directions $\Delta(i\omega)$ can be expressed from the frequency response of the machine tool $\Phi(i\omega)$ and the dynamic cutting forces $F(i\omega)$ as.

$$\begin{Bmatrix}\Delta x(i\omega)\\ \Delta y(i\omega)\end{Bmatrix}=\left(1-e^{-i\omega\tau}\right)\left[\Phi(i\omega)\right]\begin{Bmatrix}F_x(i\omega)\\ Fy(i\omega)\end{Bmatrix}$$

where

$$\Delta(i\omega)=\begin{Bmatrix}\Delta x(i\omega)\\ \Delta y(i\omega)\end{Bmatrix}=\left(1-e^{-i\omega\tau}\right)\begin{Bmatrix}x(i\omega)\\ y(i\omega)\end{Bmatrix} \tag{4.26}$$

$$\begin{Bmatrix}x(i\omega)\\ y(i\omega)\end{Bmatrix}=\left[\Phi(i\omega)\right]\begin{Bmatrix}F_x(i\omega)\\ Fy(i\omega)\end{Bmatrix}$$

Where $e^{-i\omega\tau}$ is the delay between two successive teeth. The frequency response matrix includes both direct ($\Phi_{xx}(i\omega), \Phi_{yy}(i\omega)$) and cross ($\Phi_{xy}(i\omega), \Phi_{yx}(i\omega)$) FRFs. However machine tools usually have orthogonal structures, hence cross FRFs can be neglected:

$$\left[\Phi(i\omega)\right]=\begin{bmatrix}\Phi_{xx}(i\omega) & \Phi_{xy}(i\omega)\\ \Phi_{yx}(i\omega) & \Phi_{yy}(i\omega)\end{bmatrix}=\begin{bmatrix}\Phi_{xx}(i\omega) & 0\\ 0 & \Phi_{yy}(i\omega)\end{bmatrix} \tag{4.27}$$

The dynamic cutting forces can be reduced to following:

$$\begin{Bmatrix}F_x\\ F_y\end{Bmatrix}e^{i\omega_c\tau}=\frac{1}{2}K_{tc,r}a\left[D_0\right]\left(1-e^{-i\omega_c\tau}\right)\left[\Phi(i\omega_c)\right]\begin{Bmatrix}F_x\\ Fy\end{Bmatrix}e^{i\omega_c\tau}$$

$$\begin{Bmatrix}F_x\\ F_y\end{Bmatrix}e^{i\omega_c\tau}\left[I-\frac{1}{2}K_{tc,r}a\left[D_0\right]\left(1-e^{-i\omega_c\tau}\right)\left[\Phi(i\omega_c)\right]\right]=0 \tag{4.28}$$

The characteristic equation of the system becomes

$$\det\left[I-\frac{1}{2}K_{tc,r}a\left(1-e^{-i\omega_c\tau}\right)\left[D_0\right]\left[\Phi(i\omega_c)\right]\right]=0 \tag{4.29}$$

Or in a short form as:

$$\begin{gathered}\det\left[I+\lambda\left[\Phi_0\left(i\omega_c\right)\right]\right]=0\\ \textit{where}\\ \lambda=-\frac{N}{4\pi}K_{tc,r}a\left(1-e^{-i\omega_c\tau}\right)\\ \left[\Phi_0\left(i\omega_c\right)\right]=\left[D_0\right]\left[\Phi\left(i\omega_c\right)\right]\end{gathered} \tag{4.30}$$

Which leads to the following quadratic function:

$$\begin{gathered}a_0\lambda^2+a_1\lambda+1=0\\ \textit{where}\\ a_0=\Phi_{xx}\left(i\omega_c\right)\Phi_{yy}\left(i\omega_c\right)\left(a_{xx}a_{yy}-a_{xy}a_{yx}\right)\\ a_1=a_{xx}\Phi_{xx}\left(i\omega_c\right)+a_{yy}\Phi_{yy}\left(i\omega_c\right)\end{gathered} \tag{4.31}$$

Then the eigenvalue λ is obtained as

$$\lambda=\frac{-a_1+\sqrt{{a_1}^2-4a_0}}{2a_0}=\lambda_R+i\lambda_{\mathrm{Im}} \tag{4.32}$$

The eigenvalue of the system has both real and imaginary part $\lambda=\lambda_R+i\lambda_I$. Using the $e^{-i\omega_c\tau}=\cos\omega_c\tau-\sin\omega_c\tau$ transformation and the eigenvalue given in Equation 4.32 the critical depth of cut a at the chatter frequency ω_c can be calculated as follows:

$$a=-\frac{4\pi}{NK_{tc,r}}\left[\frac{\lambda_R\left(1-\cos\omega_c\tau\right)+\lambda_{\mathrm{Im}}\sin\omega_c\tau}{\left(1-\cos\omega_c\tau\right)}+i\frac{\lambda_{\mathrm{Im}}\left(1-\cos\omega_c\tau\right)+\lambda_R\sin\omega_c\tau}{\left(1-\cos\omega_c\tau\right)}\right] \tag{4.33}$$

Since the depth of cut is a real number, the imaginary part of the Equation 4.33 vanishes $\lambda_{\mathrm{Im}}\left(1-\cos\omega_c\tau\right)+\lambda_R\sin\omega_c\tau=0$. By substituting

$$\kappa=\frac{\lambda_I}{\lambda_R}=\frac{\sin\omega_c\tau}{1-\cos\omega_c\tau} \tag{4.34}$$

Chatter free axial depth of cut is reduced to:

$$a=-\frac{2\pi}{NK_{tc,r}}[1+\kappa^2] \tag{4.35}$$

The phase distance between the inner and outer cut surface is:

$$\omega_c\tau=\pi-2\psi+2k\pi=\varepsilon+2k\pi \tag{4.36}$$

Where *k* is the integer number of waves generated within one tooth period (τ) and $\varepsilon=\pi-2\psi$ is the phase shift between the inner and outer waves. The spindle speed n (rev/min) can be is found as:

$$n=\frac{60}{N\tau} \tag{4.37}$$

Equations 4.35 and 4.37 lead to analytical prediction of critically stable depth of cuts and spindle speeds in regular milling operations. However as the radial engagement boundaries in orbital drilling process vary throughout the tool diameter as shown in Chapter 3, which brings additional delays and varying directional coefficients depending on the cutting conditions and speed. As a result, the frequency domain, analytical solution presented by Altintas and Budak [27] may not always lead to accurate solutions for the stability of orbital drilling operations. By considering the spindle speed, Nyquist stability criterion is used in this thesis as illustrated in Figure 4.5[35][36].

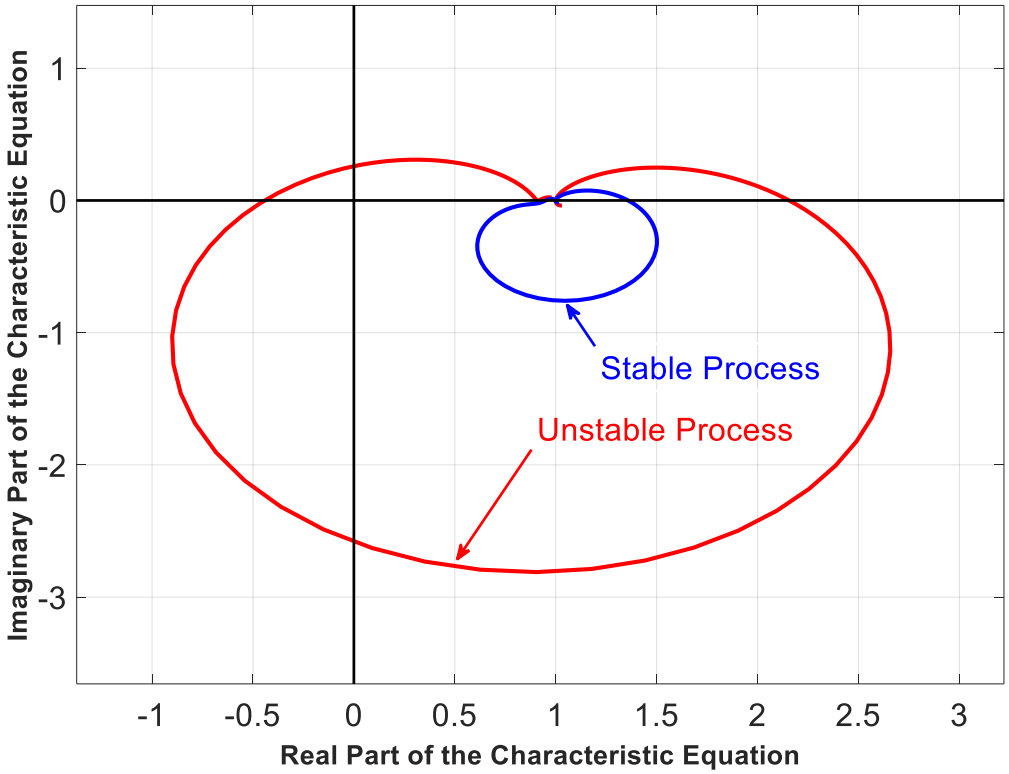

Figure 4.5 Nyquist plot of the characteristic equation for stable and unstable process

The Nyquist stability criterion sweeps around the most flexible modes of the structure and looks clock-wise encirclements of the complex plane origin as illustrated in Figure 4.5. If the Nyquist plot encircles the origin, it means unstable process.

The stability lobes are searched at different pitch lengths of tool path (a_p) and spindle speed (n) pairs. The radial engagement profile changes at each different pitch length, hence it is required to calculate the most severe radial engagement in second zone, first. Then the calculated engagement area is discretized into segments as shown in Figure 4.6.

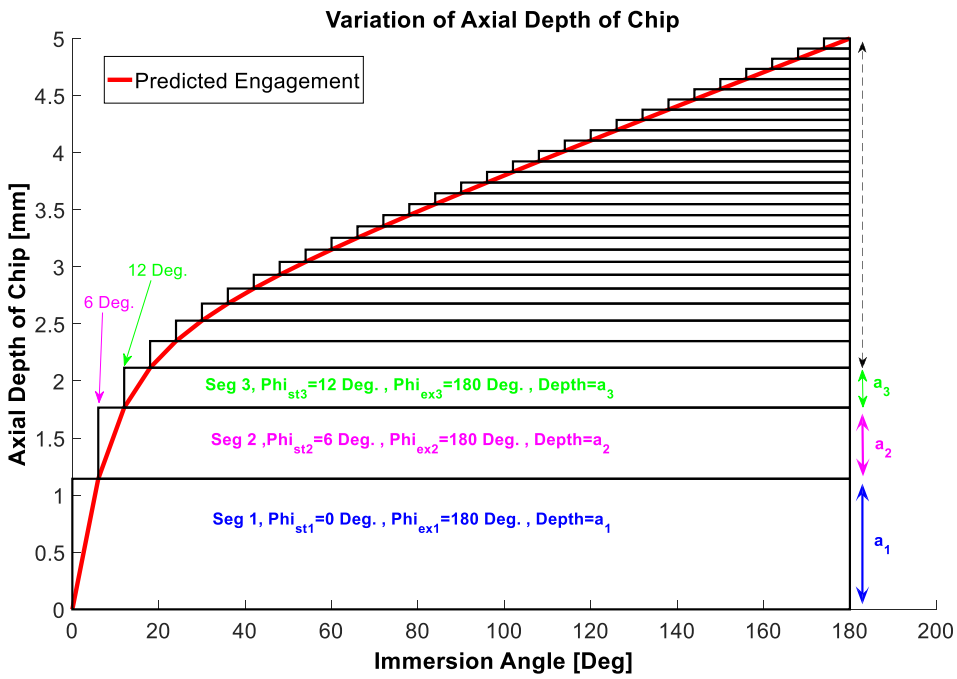

Figure 4.6 Predicted and discretized radial engagement profile for the case where Tool Dia.=16mm, Hole Dia.=30 mm, Pitch Length=5 mm, Discretization Angle: 6 deg.

After discretizing the radial engagement into different segments, the characteristic equation of each segment can be written as follows:

$$\det\left[I-\frac{1}{2}K_{tc,r}a_i\left(1-e^{-i\omega_c\tau}\right)\left[D_{0,i}\right]\left[\Phi\left(i\omega_c\right)\right]\right]=0 \tag{4.38}$$

Where $\left[D_{0,i}\right]=\left[D_0\right]_{\phi_{st,r,i}}^{\phi_{ex,r,i}}$ is the coefficient matrix and a_i is the height of each segment. The characteristic equation for each pitch length (a_p) and spindle speed (n) pair can then be expressed as :

$$\det\left[I-\frac{1}{2}K_{tc,r}\left(1-e^{-i\omega_c\tau}\right)\left[D_T\right]\left[\Phi\left(i\omega_c\right)\right]\right]=0$$

$$\textit{where} \tag{4.39}$$

$$D_T=\sum_{i=1}^{K}\left[D_{0,i}\right]a_i$$

The characteristic equation of each case is assessed by the Nyquist stability criterion and then stability lobes are generated for different pitch lengths.

4.3.3 Chatter Stability in Semi-Discrete Time Domain Solution

Stability of the milling was predicted by extending semi-discretization method proposed by Stepan et al.[37,38]. If the machines structural flexibilities are assumed to be orthogonal, the FRF of the lateral directions can be represented as follows:

$$\Phi_{xx}(s)=\frac{\omega^2{}_{nx}/(k_x)}{s^2+2\xi_x\omega_{nx}s+\omega^2{}_{nx}} \rightarrow \ddot{x}(t)+2\xi_x\omega_{nx}\dot{x}(t)+\omega^2{}_{nx}x(t)=\frac{\omega^2{}_{nx}}{k_x}F_x(t)$$
$$\Phi_{yy}(s)=\frac{\omega^2{}_{ny}/(k_y)}{s^2+2\xi_y\omega_{ny}s+\omega^2{}_{ny}} \rightarrow \ddot{y}(t)+2\xi_y\omega_{ny}\dot{y}(t)+\omega^2{}_{ny}y(t)=\frac{\omega^2{}_{ny}}{ky}F_y(t) \quad (4.40)$$

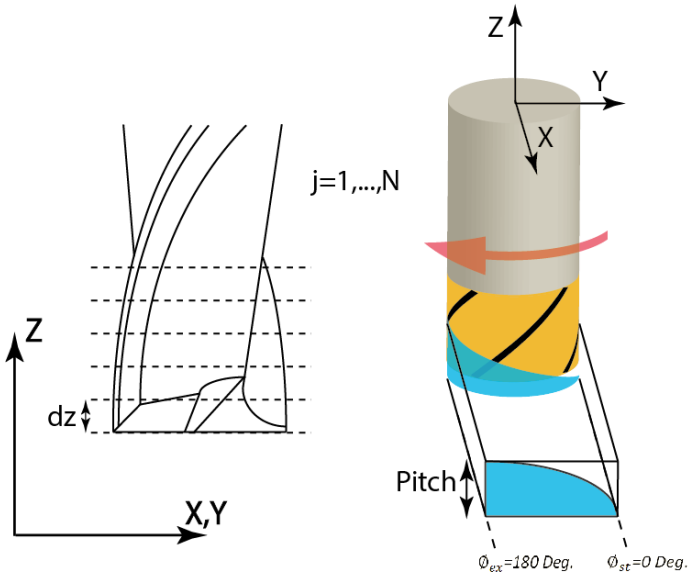

Figure 4.7 Discretized tool geometry(left) and a sample radial engagement(right)

The end mill is discretized into differential segments with uniform height of *dz* as it is shown in Figure 4.7. The dynamic forces inn x and y directions at each segment can be expressed as:

$$\begin{Bmatrix} F_x(t) \\ F_y(t) \end{Bmatrix} = \frac{1}{2} dz K_{tc,r} \begin{bmatrix} a_{xx} & a_{xy} \\ a_{yx} & a_{yy} \end{bmatrix} \left(\begin{Bmatrix} x(t) \\ y(t) \end{Bmatrix} - \begin{Bmatrix} x(t-\tau) \\ y(t-\tau) \end{Bmatrix} \right) \tag{4.41}$$

which is valid if the cutting flute at a specific segment is in cut, i.e. within engagement boundaries. The dynamics of the cutting at each differential segment is expressed as,

$$\begin{Bmatrix} \ddot{x}(t) + 2\xi_x \omega_{nx} \dot{x}(t) + \omega^2{}_{nx} x(t) \\ \ddot{y}(t) + 2\xi_y \omega_{ny} \dot{y}(t) + \omega^2{}_{ny} y(t) \end{Bmatrix} = \frac{1}{2} dz K_{tc,r} \begin{bmatrix} \omega^2{}_{ny}/k_x & 0 \\ 0 & \omega^2{}_{ny}/k_y \end{bmatrix} \begin{bmatrix} a_{xx} & a_{xy} \\ a_{yx} & a_{yy} \end{bmatrix} \left(\begin{Bmatrix} x(t) \\ y(t) \end{Bmatrix} - \begin{Bmatrix} x(t-\tau) \\ y(t-\tau) \end{Bmatrix} \right) \tag{4.42}$$

Or in matrix as follows:

$$\begin{bmatrix} 1 & 0 \\ 0 & 1 \end{bmatrix} \begin{Bmatrix} \ddot{x} \\ \ddot{y} \end{Bmatrix} + \begin{bmatrix} 2\xi_x \omega_{nx} & 0 \\ 0 & 2\xi_y \omega_{ny} \end{bmatrix} \begin{Bmatrix} \dot{x} \\ \dot{y} \end{Bmatrix} + \begin{bmatrix} \omega^2{}_{nx} & 0 \\ 0 & \omega^2{}_{ny} \end{bmatrix} \begin{Bmatrix} x \\ y \end{Bmatrix} = \frac{1}{2} dz K_{tc,r} \begin{bmatrix} \omega^2{}_{ny}/k_x & 0 \\ 0 & \omega^2{}_{ny}/k_y \end{bmatrix} \begin{bmatrix} a_{xx} & a_{xy} \\ a_{yx} & a_{yy} \end{bmatrix} \left(\begin{Bmatrix} x(t) \\ y(t) \end{Bmatrix} - \begin{Bmatrix} x(t-\tau) \\ y(t-\tau) \end{Bmatrix} \right) \tag{4.43}$$

The two sets of second order delayed differential equations are reduced to state space form as:

$$\begin{aligned} x_1 = x(t), x_2 = \frac{dx(t)}{dt}, \dot{x}_1 = x_2 \\ y_1 = y(t), y_2 = \frac{dy(t)}{dt}, \dot{y}_1 = y_2 \end{aligned} \tag{4.44}$$

First order representation of the system becomes

$$\begin{aligned} \{\dot{q}\} = [L]\{q\} + [R]\{q(t-\tau)\} \\ \{q_i(t-\tau)\} \end{aligned} \tag{4.45}$$

where

$$\{q\}=\begin{Bmatrix} x(t) \\ y(t) \\ \dot{x}(t) \\ \dot{y}(t) \end{Bmatrix},\ [D(t)]=\begin{bmatrix} a_{xx}(t) & a_{xy}(t) \\ a_{yx}(t) & a_{yy}(t) \end{bmatrix},\ \delta=\frac{1}{2}dzK_{tc,r}$$

$$[M]^{-1}=\begin{bmatrix} \omega^2{}_{ny}/k_x & 0 \\ 0 & \omega^2{}_{ny}/k_y \end{bmatrix},\ [C]=\begin{bmatrix} -2\xi_x\omega_{nx} & 0 \\ 0 & -2\xi_y\omega_{ny} \end{bmatrix},\ [\Gamma]=\begin{bmatrix} \omega^2{}_{nx} & 0 \\ 0 & \omega^2{}_{ny} \end{bmatrix} \quad (4.46)$$

$$[L]^{-1}=\begin{bmatrix} [0]_{2x2} & [I]_{2x2} \\ -\delta[M]^{-1}[D(t)]-[\Gamma] & [C] \end{bmatrix},\ [R]=\begin{bmatrix} [0] & [0] \\ -\delta[M]^{-1}[D(t)] & [0] \end{bmatrix}$$

The tooth period τ is discretized into small time intervals Δt as shown in Figure 4.8. Current state at time t_i is represented by $\{q_i\}$ where the state a tooth period before is represented by $\{q_i(t-\tau)\}$.

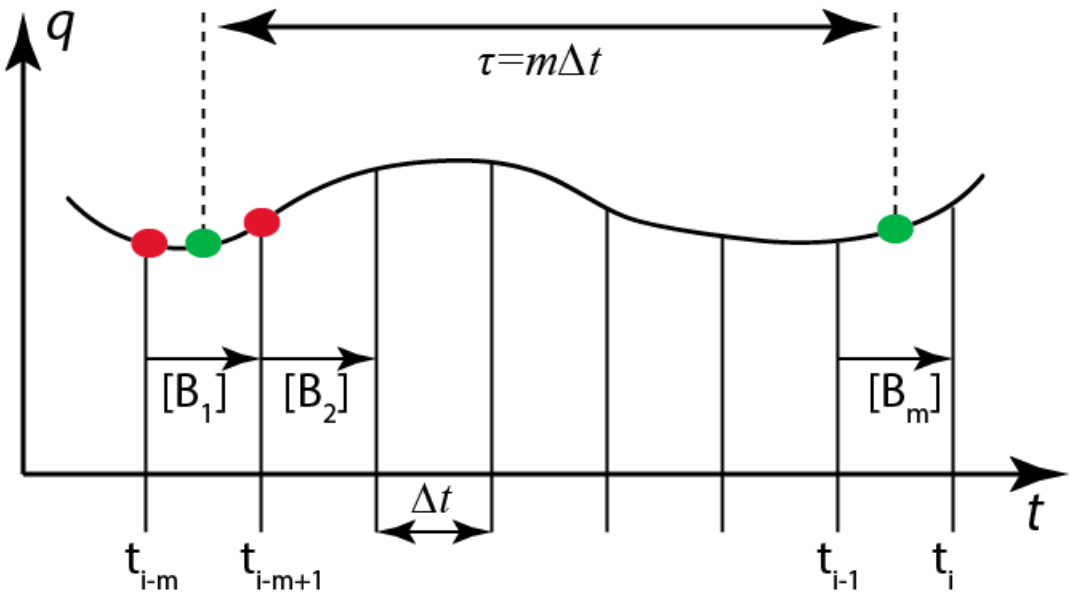

Figure 4.8 Semi-discretization of tooth period

If the time interval Δt is very small, the states $\{q\}$ can be defined as the average of two consecutive states as given as:

$$\{q(t-\tau)\} \approx \frac{\{q(t_i-\tau+\Delta t)\}+\{q(t_i-\tau)\}}{2} = \frac{\{q_{i-m+1}\}-\{q_{i-m}\}}{2} \tag{4.47}$$

The dynamics of the system can be rewritten at discrete time intervals as:

$$\{\dot{q}_i\} = [L_i]\{q_i\} + \frac{1}{2}[R_i](\{q_{i-m+1}\}-\{q_{i-m}\}) \tag{4.48}$$

The differential Equation 4.48 has homogeneous $\{q_{i,h}(t)\}$ and particular $\{q_{i,\mathrm{p}}(t)\}$ solutions. The details of the semi-discrete solution can be found in [32].

$$\{q_i(t)\} = \{q_{i,h}(t)\} + \{q_{i,\mathrm{p}}(t)\} \tag{4.49}$$

The state solution at time $t = t_{i+1}$ is given as:

$$\{q_{i+1}\} = e^{[L_i]\Delta t}\{q_i\} + \frac{1}{2}([L_i]\Delta t - [I])[L_i]^{-1}[R_i](\{q_{i-m+1}\}+\{q_{i-m}\}) \tag{4.50}$$

Where $\Delta t = t_{i+1} - t_i$ and $t = t_{i+1}$. Equation 4.50 requires the previous value of the state $\{q_i\}$ and values of the state a delay before $(\{q_{i-m+1}\},\{q_{i-m+1}\})$. Equation 4.50 can be expressed as follows:

$$\{z_{i+1}\} = [B_i]\{z_i\} \tag{4.51}$$

where

$$\{z_i\} = \begin{Bmatrix} \{q_i\} \\ \{q_{i-1}\} \\ \vdots \\ \{q_{i-m+1}\} \\ \{q_{i-m}\} \end{Bmatrix}_{(m+1)x1}$$

$$[B_i] = \begin{bmatrix} e^{[L_i]\Delta t} & [0] & \cdots & \frac{1}{2}\left(e^{[L_i]\Delta t} - [I]\right)[L_i]^{-1}[R_i] & \frac{1}{2}\left(e^{[L_i]\Delta t} - [I]\right)[L_i]^{-1}[R_i] \\ [I] & [0] & \cdots & [0] & [0] \\ [0] & [I] & \cdots & \vdots & \vdots \\ \vdots & \vdots & \ddots & [0] & [0] \\ [0] & [0] & [0] & [I] & [0] \end{bmatrix}_{4[m+1]x4[m+1]} \quad (4.52)$$

The stability of the process can be assessed for one tooth period τ with m number of discrete time intervals as:

$$\{z_{i+m}\} = [\Psi]\{z_i\} = [B]_m \ldots [B]_2 [B]_1 \{z_i\} \quad (4.53)$$

According to Floquet's linear periodic system theory, the system is defined as unstable if any of the eigenvalues of the transition matrix $[\Psi]$ have a modulus greater than one, critically stable if the modulus is equal to one, and stable if the moduluses of all the eigenvalues are less than one. The stability lobes are obtained by checking different pitch length spindle speed pairs as carried out in Nyquist method. However, semi-discrete method considers time varying directional coefficients which are averaged and assumed to be time independent when Nyquist approach is used for the stability.

The equations given above are valid when one dominant mode is considered for each direction. However when there are N_m number of dominant modes for each direction, $[M]^{-1}$, $[C]$ and $[\Gamma]$ matrices should be expanded as follows:

$$[M]^{-1}=\begin{bmatrix} \omega^2_{nx_1}/k_{x_1} & 0 & 0 & & \\ 0 & \ddots & 0 & [0]_{(N_m)x(N_m)} & \\ 0 & 0 & \omega^2_{nx_{N_m}}/k_{x_{N_m}} & & \\ & & & \omega^2_{ny_1}/k_{y_1} & 0 & 0 \\ [0]_{(N_m)x(N_m)} & & & 0 & \ddots & 0 \\ & & & 0 & 0 & \omega^2_{ny_{N_m}}/k_{y_{N_m}} \end{bmatrix}_{(2N_m)x(2N_m)}$$

$$[C]=\begin{bmatrix} -2\xi_{x_1}\omega_{nx_1} & 0 & 0 & & \\ 0 & \ddots & 0 & [0]_{(N_m)x(N_m)} & \\ 0 & 0 & -2\xi_{x_{N_m}}\omega_{nx_{N_m}} & & \\ & & & -2\xi_{y_1}\omega_{ny_1} & 0 & 0 \\ [0]_{(N_m)x(N_m)} & & & 0 & \ddots & 0 \\ & & & 0 & 0 & -2\xi_{y_{N_m}}\omega_{ny_{N_m}} \end{bmatrix}_{(2N_m)x(2N_m)}$$

$$[\Gamma]=\begin{bmatrix} \omega^2_{nx_1} & 0 & 0 & & \\ 0 & \ddots & 0 & [0]_{(N_m)x(N_m)} & \\ 0 & 0 & \omega^2_{nx_{N_m}} & & \\ & & & \omega^2_{ny_1} & 0 & 0 \\ [0]_{(N_m)x(N_m)} & & & 0 & \ddots & 0 \\ & & & 0 & 0 & \omega^2_{ny_{N_m}} \end{bmatrix}_{(2N_m)x(2N_m)} \tag{4.54}$$

The procedure for the rest of the solution is identical to what is given for the one dominant mode case.

Results of stability solution is given for a sample case in Figure 4.9 when the end mill is at θ = 0 [deg.]

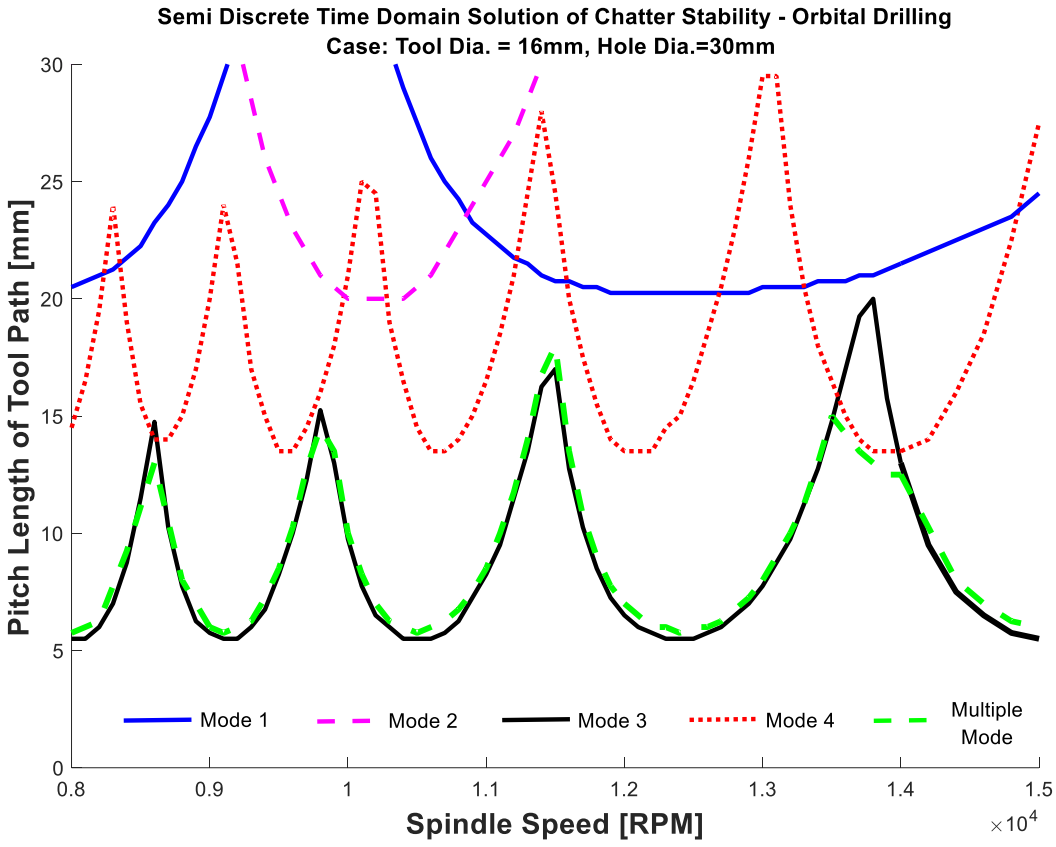

Figure 4.9 Semidiscrete time domain stability lobes for orbital drilling process. Tool Dia.=16 [mm], Hole Dia.= 30 [mm], Helix Angle = 25 [deg], $\boldsymbol{K_{tc,r}}$ = 900 [MPa], $\boldsymbol{K_{rc,r}}$ = 270 [MPa], modal parameters taken from [39]. $\boldsymbol{w_{nx1}}$= 624 [Hz] , $\boldsymbol{\xi_{x1}}$ = 0.052 , $\boldsymbol{k_{x1}}$ = 8.2 x $\mathbf{10^7}$ [N/m], $\boldsymbol{w_{nx2}}$= 871 [Hz] , $\boldsymbol{\xi_{x2}}$ = 0.033 , $\boldsymbol{k_{x2}}$ = 16.1 x $\mathbf{10^7}$ [N/m], $\boldsymbol{w_{nx3}}$= 2311 [Hz] , $\boldsymbol{\xi_{x3}}$ = 0.022, $\boldsymbol{k_{x3}}$ = 8.7 x $\mathbf{10^7}$ [N/m], $\boldsymbol{w_{nx4}}$= 3052 [Hz] , $\boldsymbol{\xi_{x4}}$ = 0.029 , $\boldsymbol{k_{x4}}$ = 14.5 x $\mathbf{10^7}$ [N/m], $\boldsymbol{w_{ny1}}$= 692 [Hz] , $\boldsymbol{\xi_{y1}}$ = 0.042, $\boldsymbol{k_{y1}}$ = 7.6 x $\mathbf{10^7}$ [N/m], $\boldsymbol{w_{ny2}}$= 862 [Hz] , $\boldsymbol{\xi_{y2}}$ = 0.052 , $\boldsymbol{k_{y2}}$ = 13.5 x $\mathbf{10^7}$ [N/m], $\boldsymbol{w_{ny3}}$= 2289 [Hz], $\boldsymbol{\xi_{y3}}$ = 0.019, $\boldsymbol{k_{y3}}$ = 7.9 x $\mathbf{10^7}$ [N/m], $\boldsymbol{w_{ny4}}$= 3050 [Hz], $\boldsymbol{\xi_{y4}}$ = 0.027 , $\boldsymbol{k_{y4}}$ = 15.0 x $\mathbf{10^7}$ [N/m]

The multiple mode solution considers the flexibilities of all modes of the end mill.

4.4 Oriented Frequency Response Function

The methods that presented so far assess the stability of the system at one point however during orbital drilling operation the feed direction of the end mill changes as the tool moves around the hole center as it is shown in Figure 4.10.

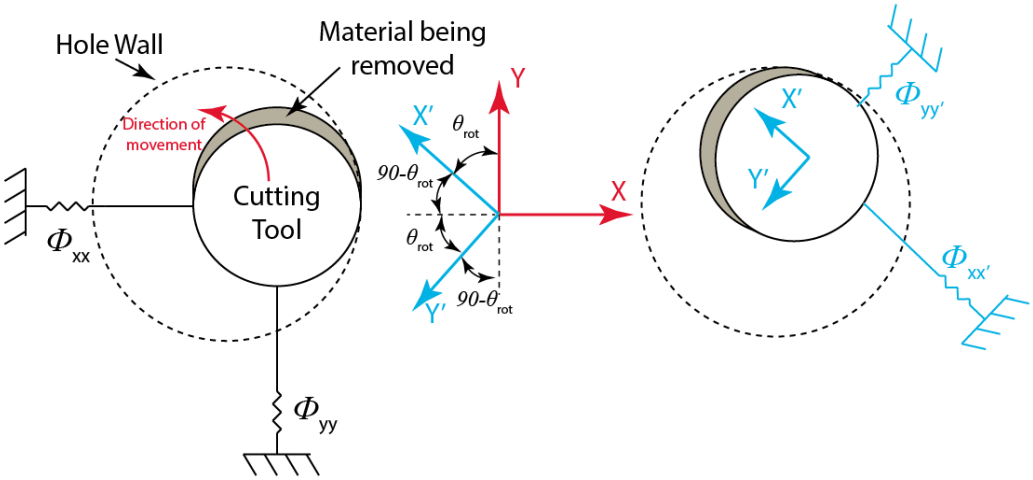

Figure 4.10 Frequency response on local and global coordinates

Koenigsberger and Tlusty [40] defined the frequency response function between cutting forces and the resultant vibration directions (X',Y') as oriented FRFs. Hence, the FRFs on global coordinates $\left(\Phi_{xx},\Phi_{yy}\right)$ has to be projected to the feed and normal directions as the tool follows orbital drilling path. The projected frequency responses along instantaneous feed and normal direction $\left(\Phi_{xx'},\Phi_{yy'}\right)$ of the end mill can be evaluated as:

$$\begin{aligned}\Phi_{xx'} &= \Phi_{xx}\cos^2(90+\theta)+\Phi_{yy}\cos^2(\theta)\\ \Phi_{yy'} &= \Phi_{xx}\cos^2(180+\theta)+\Phi_{yy}\cos^2(90+\theta)\end{aligned} \tag{4.55}$$

4.5 Simulations and Experimental Results

A set of orbital drilling experiments have been carried out a range of hole pitch lengths and spindle speeds listed in Table 4.2.

An end mill with radius R_T = 8 [mm], pitch angle β_h = 25 [deg] and N = 2 teeth has been used for opening holes with D_H = 30 [mm] diameter. The workpiece material is Al7050-T7451 with the experimentally identified cutting coefficients $K_{tc,r}$ = 752.4 [MPa] and $K_{rc,r}$ = 178.3 [MPa]. The presence of chatter has been detected from the spectrum of sound and hole surface. If the spectrum peaks close to one of the natural frequencies of the machine, with peaks spindle/tooth passing frequencies away on the left and right, the presence of chatter is assumed. The presence of forced vibrations is decided when the spectrum is dominated by the spindle and/or tooth passing frequencies and their harmonics.

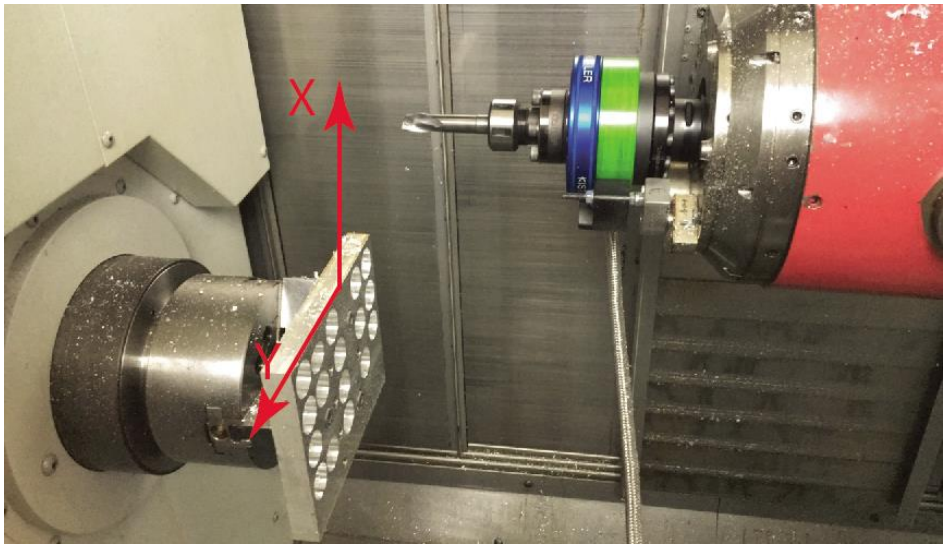

Figure 4.11 Experimental setup for chatter tests

Modal parameters of the structures in x and y directions are given in Table 4.1. FRF's on the tool tip are given in Figure 4.12.

Table 4.1 Modal parameters at the tool tip

Measurement Direction	Natural Frequency [Hz]	Damping Ratio ξ	Stiffness k [N/m]
X	376.6, 503.9, 1008.1, 1241.5, 1584.7, 1821.1, 2357.8, 3554.9, 4574.7	0.0251, 0.0927, 0.0351, 0.0245, 0.0461, 0.0277, 0.0769, 0.0291, 0.0214	2.31e7, 1.50e7, 5.19e7, 5.49e7, 2.59e7, 4.26e8, 2.58e7, 3.41e8, 2.58e8
Y	443.4, 522.6, 996.1, 1138.9, 1344.1, 1608.0, 2369.3, 3818.8, 4586.8	0.0797, 0.0657, 0.0729, 0.0687, 0.0500, 0.0320, 0.0589, 0.0366, 0.0243	1.57e7, 1.42e7, 4.25e7, 8.81e7, 9.62e7, 4.28e7, 3.07e7, 3.81e8, 2.76e8

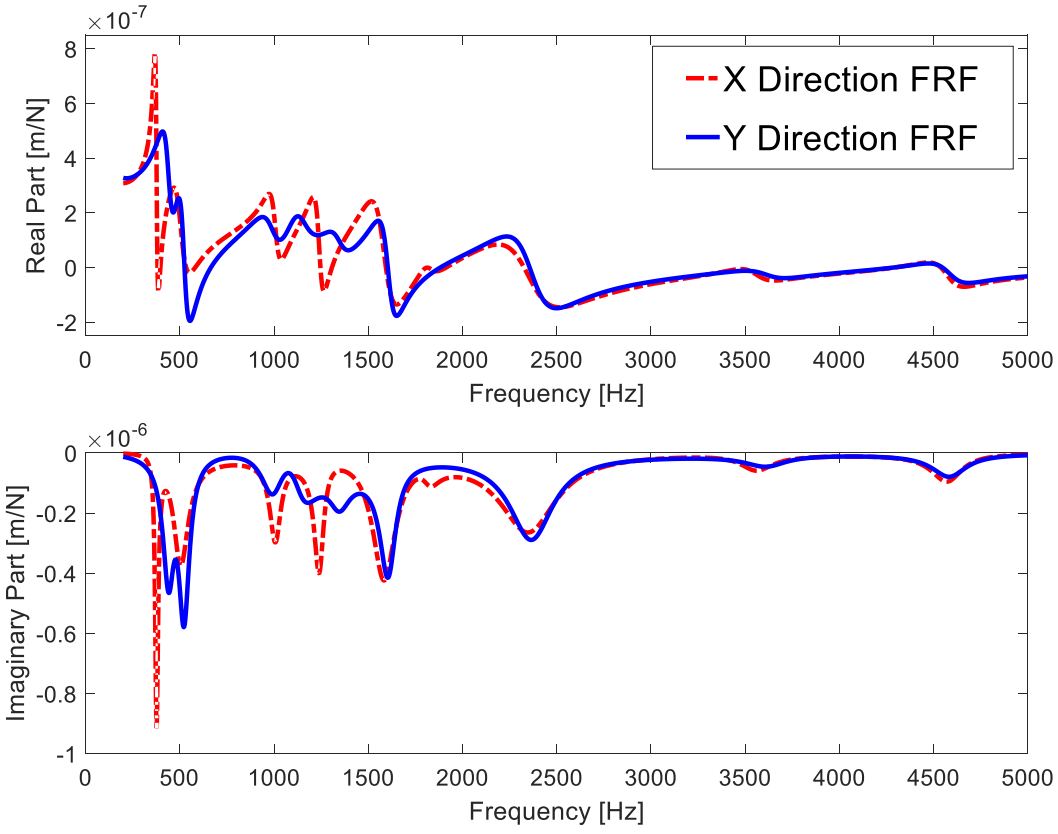

Figure 4.12 Two orthogonal direction FRF's at the tool tip

Table 4.2 Pitch length of tool path (a_p) and spindle speed (n) values for chatter tests

Experiments	Spindle Speed [RPM]	Orbital Speed [RPM]	Pitch of Tool Path [mm]	Tangential Feed of the Tool [mm/tooth]	Axial Feed of the Tool [mm/tooth]
# 1.	8000	10	3	0.0275	0.002
# 2.	8000	10	5	0.0275	0.003
# 3.	8000	10	6	0.0275	0.0037
# 4.	8400	10.5	3	0.0275	0.002
# 5.	8400	10.5	4	0.0275	0.0025
# 6.	8400	10.5	5	0.0275	0.003
# 7.	8400	10.5	6	0.0275	0.0037
# 8.	8800	11	3	0.0275	0.002
# 9.	8800	11	4	0.0275	0.0025
# 10.	8800	11	5	0.0275	0.003
# 11.	8800	11	6	0.0275	0.0037
# 12.	9200	11.5	2.5	0.0275	0.0016
# 13.	9200	11.5	4	0.0275	0.0025
# 14.	9200	11.5	5	0.0275	0.003
# 15.	9200	11.5	6	0.0275	0.0037

FRFs have been oriented as the feed direction changes along the orbital tool path. Sample oriented FRFs for feeds with $\theta = 45\,\text{deg}$ are given for X and Y directions in Figure 4.13 and Figure 4.14 respectively.

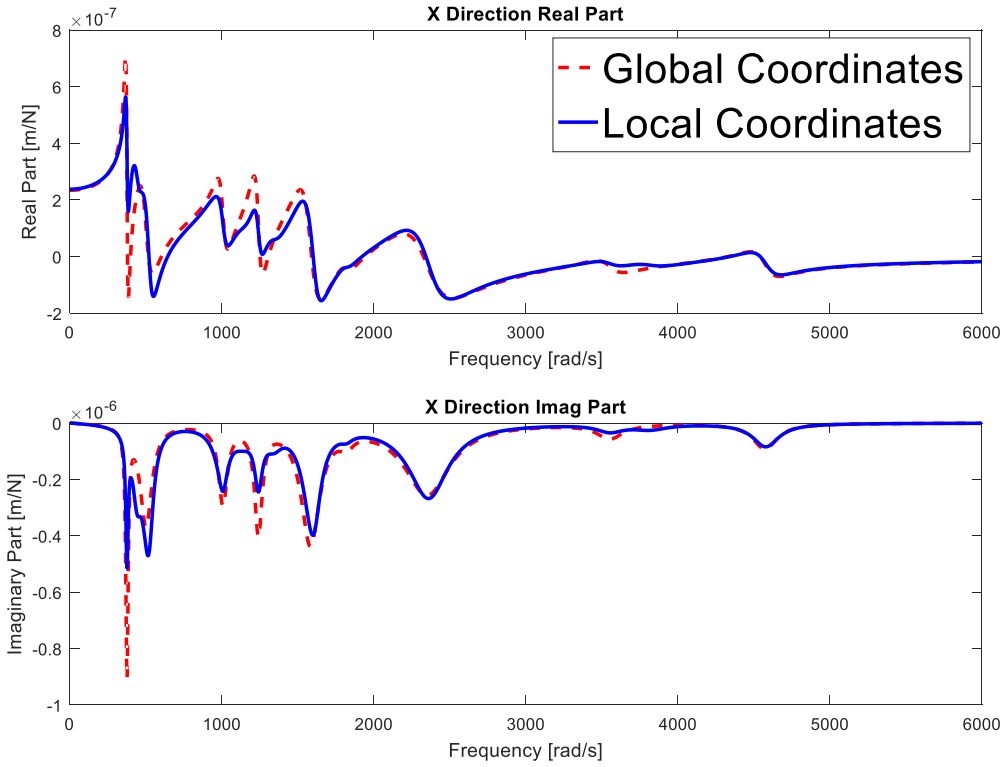

Figure 4.13 FRF on global and local X coordinates of end mill when $\boldsymbol{\theta}$ = 45 deg.

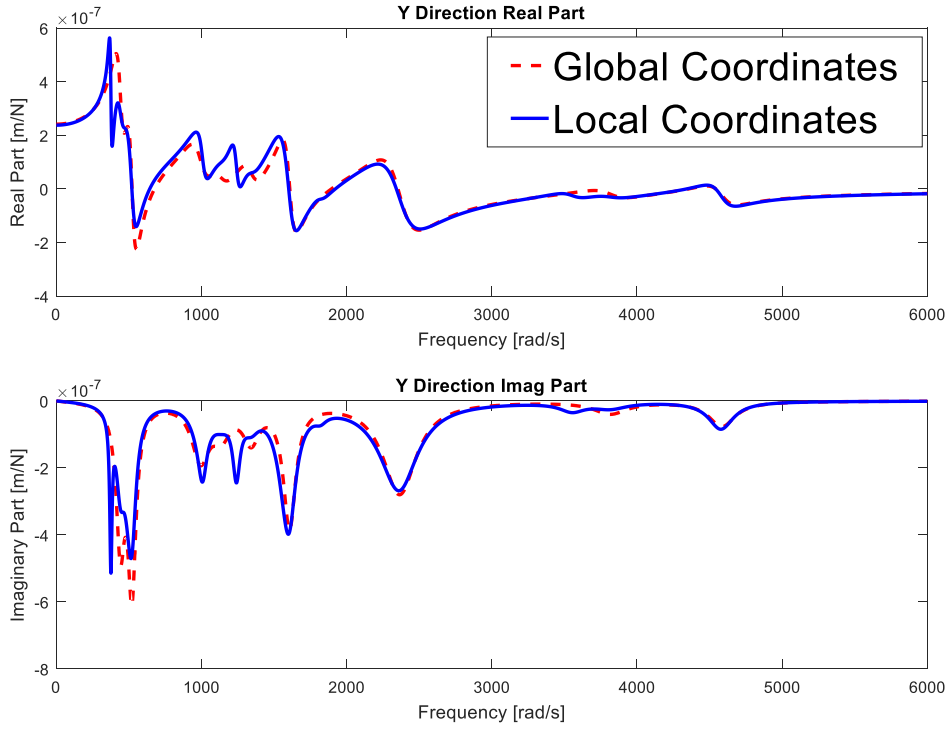

Figure 4.14 FRF on global and local Y coordinates of end mill when $\boldsymbol{\theta}$ = 45 deg.

Sound measurements and the corresponding spectrums are shown along the orbital drilling path starting at $\theta = 0$ degree and completing the full hole at $\theta = 360$ degrees. A stable orbital drilling process carried out at the spindle speed of 8000 rev/min is shown in Figure 4.15. The spectrum is dominated by the spindle frequency (133.33Hz) due to run out, tooth passing frequency (266.7 Hz) and their harmonics which indicate forced vibrations hence the stability. The visually observed surface finish was also smooth. Sample, unstable orbital drilling test results are shown in Figure 4.16 where the system chatters close to 522 Hz natural mode. The spectrums are spread to the right and left with integer number (*k*) of tooth passing frequencies away (i.e. $\omega_c \pm k\omega_T$) which indicates the presence of chatter. The hole surface was also observed to be rough containing chatter marks.

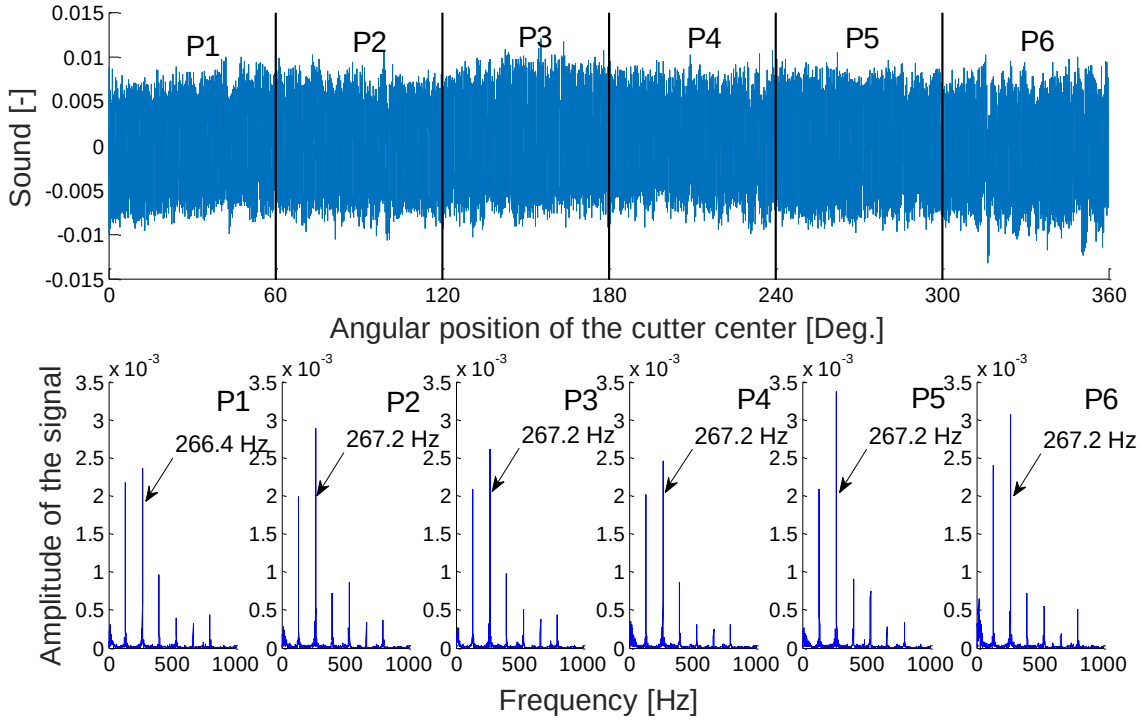

Figure 4.15 Stable orbital drilling: Measured sound signals and their FFT for $\boldsymbol{a_p}$ = 3mm, $\boldsymbol{n}$ = 8000 RPM, $\boldsymbol{s_{tan}}$ = 0.0275 mm/tooth, $\boldsymbol{s_{ax}}$ = 0.002 mm/tooth, Tooth Passing Frequency=266.7 Hz

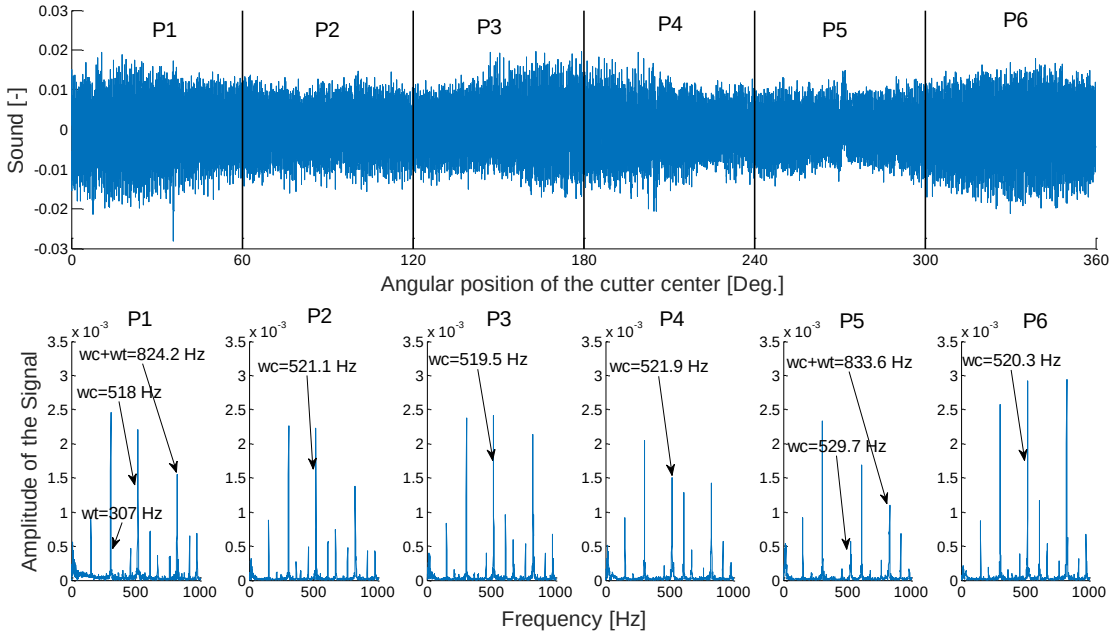

Figure 4.16 Unstable orbital drilling: Measured sound signals and their FFT for a_p = 6mm, n = 9200 RPM, s_{tan} = 0.0275 mm/tooth, s_{ax} = 0.0037 mm/tooth, Tooth Passing Frequency=306.7 Hz

The predicted stability charts have been experimentally validated by recording the sound from a microphone attached close to the cuting zone. The assesment of stable and unstable process was made when the end mill starts cutting in zone 2, where the radial engagement reaches its maximum.

Frequency domain solution requires FRF of the structure in feed and normal directions whereas the semi-discrete time domain solution requires the modal parameters of the system in each direction. Regarding the feed direction change during the orbital drilling process, calculation of modal parameters in both directions at each predefined point is necessary for solving the 3D chatter stability of the operation in time domain. Besides, if higher number of the modes of the structure is included in the time domain solution, the solution starts being time consuming since the matrixes corresponding with the modal parameters start expanding.

Therefore, it is decided to solve the stability of the system in frequency domain in order to observe the dominant modes around the experiment points.

The chatter stability diagram (Figure 4.17) is obtained in Frequency Domain as functions of spindle speed, angular position of the tool and pitch length of the tool path.

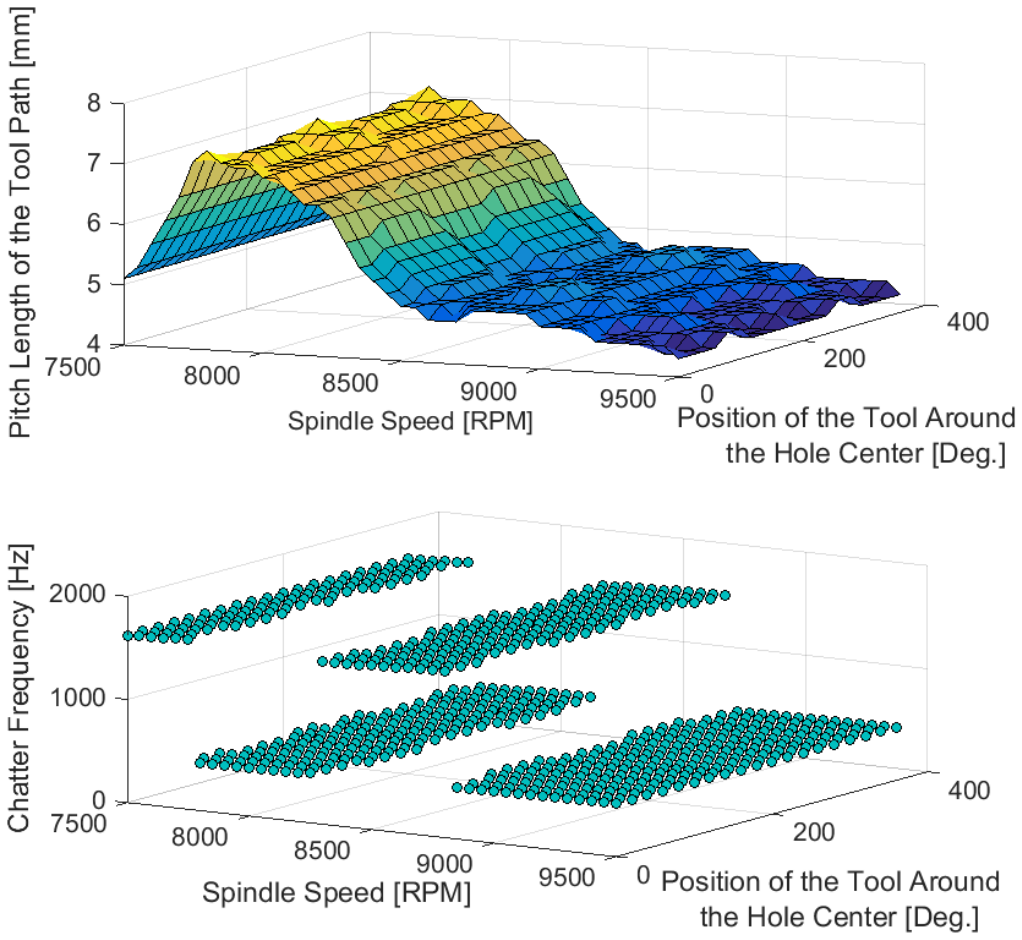

Figure 4.17 3D stability lobe for orbital drilling and chatter simulated chatter frequencies/Nyquist solution

Results of the experiments and simulation can be better compared on a two dimensional graph when the tool is at $\theta = 0$ deg and when n=9200 rpm as shown in Figure 4.18 and Figure 4.19.

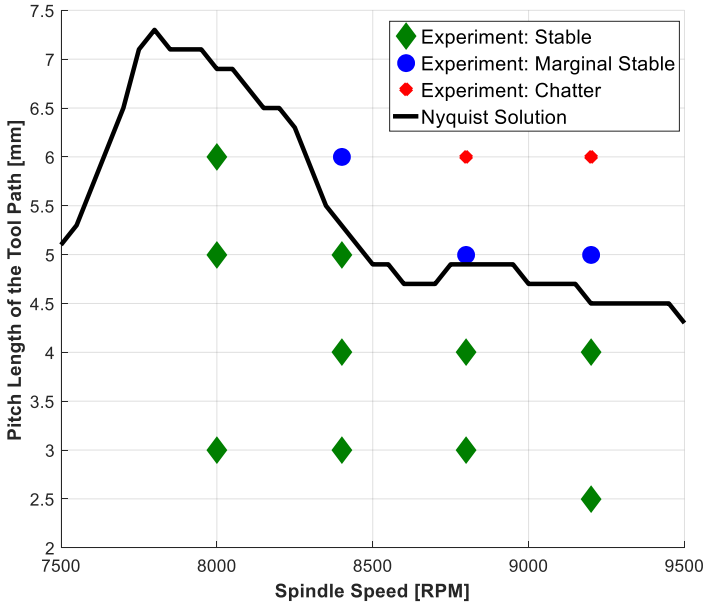

Figure 4.18 Comparison of Nyquist solution and experimentally measured chatter stability when end mill is at $\boldsymbol{\theta}$ = 0 deg

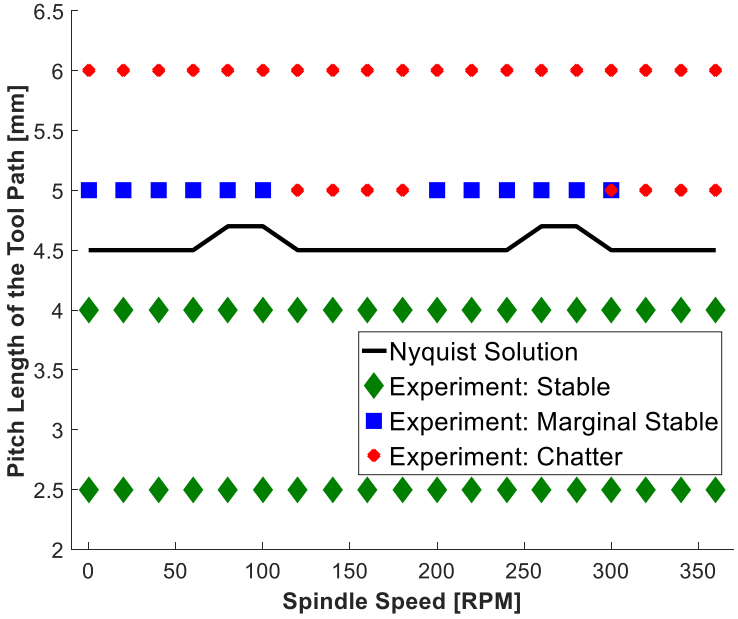

Figure 4.19 Stability limits during the rotation of the tool around the hole center for $\boldsymbol{n}$ = 9200 RPM/ Nyquist solution

Frequency domain solution and the experimental results are in great agreement. Furthermore, from the frequency domain solution it is observed that when the spindle speed changes between 7500 rpm and 9500 rpm the dominant natural frequencies of the structure are around 500 Hz and 1600 Hz. That's why time domain simulation considers the modal parameters given on Table 4.3.

Table 4.3 Modal parameters for semi-discrete time domain solution

Direction	Natural Frequency [Hz]	Damping Ratio ξ	Stiffness k [N/m]
X	503.9, 1584.8	0.0927, 0.0461	1.50e7, 2.59e7
Y	522.6, 1608	0.0657, 0.0320	1.42e7, 4.28e7

The chatter stability diagram (Figure 4.20) is obtained in Semi-Discrete Time Domain as functions of spindle speed, angular position of the tool and pitch length of the tool path.

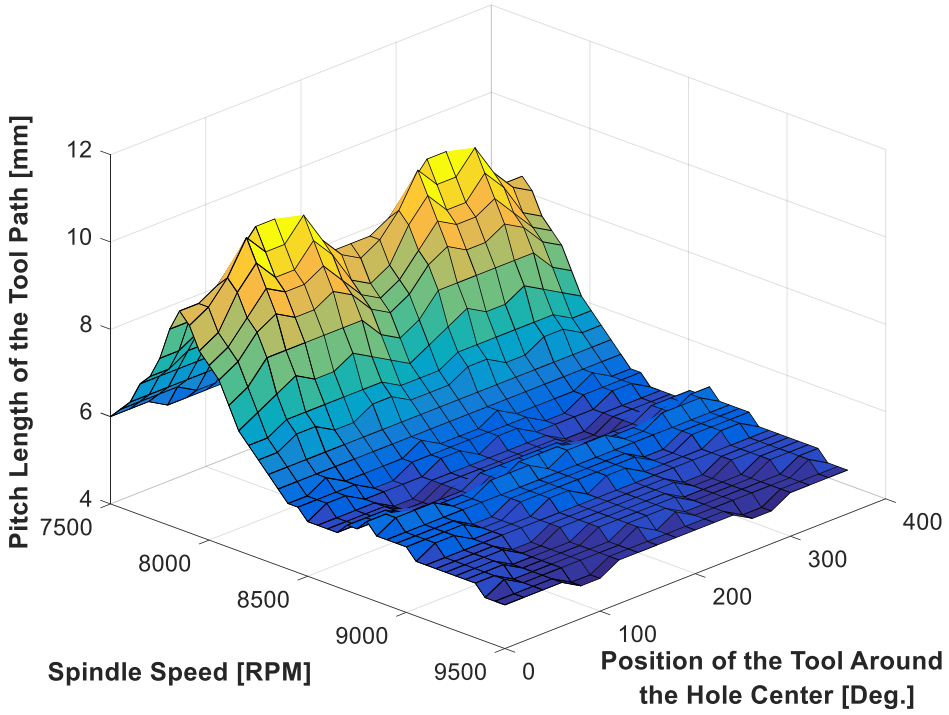

Figure 4.20 3D stability lobe for orbital drilling /Semi-discrete time domain solution

Time domain and frequency domain solutions can be better compared on a two dimensional graph when the tool is at $\theta = 0$ deg as shown in Figure 4.21.

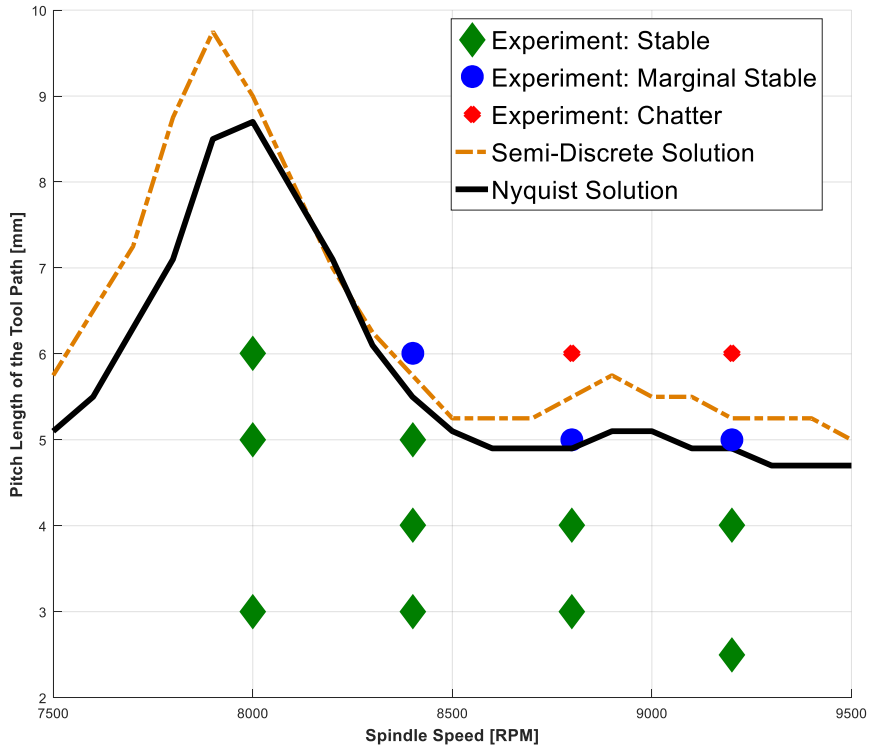

Figure 4.21 Comparison of predicted and experimentally measured chatter stability when end mill is at $\boldsymbol{\theta}$ = 0 deg

The frequency and time domain results have small discrepancies and they show consistency with the experimental results. The radial engagement profile is discretized into segments and average directional coefficient matrix for each segment is calculated with the zero order frequency domain method. However as the engagement area gets smaller, the averaging of directional coefficients lead to errors. On the other hand, semi discrete time domain solution considers the cutters exact rotation within the engagement, hence time varying directional coefficients are considered, hence leads to more accurate solutions.

Frequency and time domain simulation results are computed at each 20 degrees rotation of the end mill around hole center with 50 rpm intervals. Both solution algorithms are implemented on Matlab R2016a platform. Nyquist solution that considers all of the natural frequencies in both lateral directions takes seventy six minutes whereas Nyquist solution that considers only two modes, takes thirty two minutes. Semi-discrete time domain solution that considers two modes takes three hundred and one minutes.

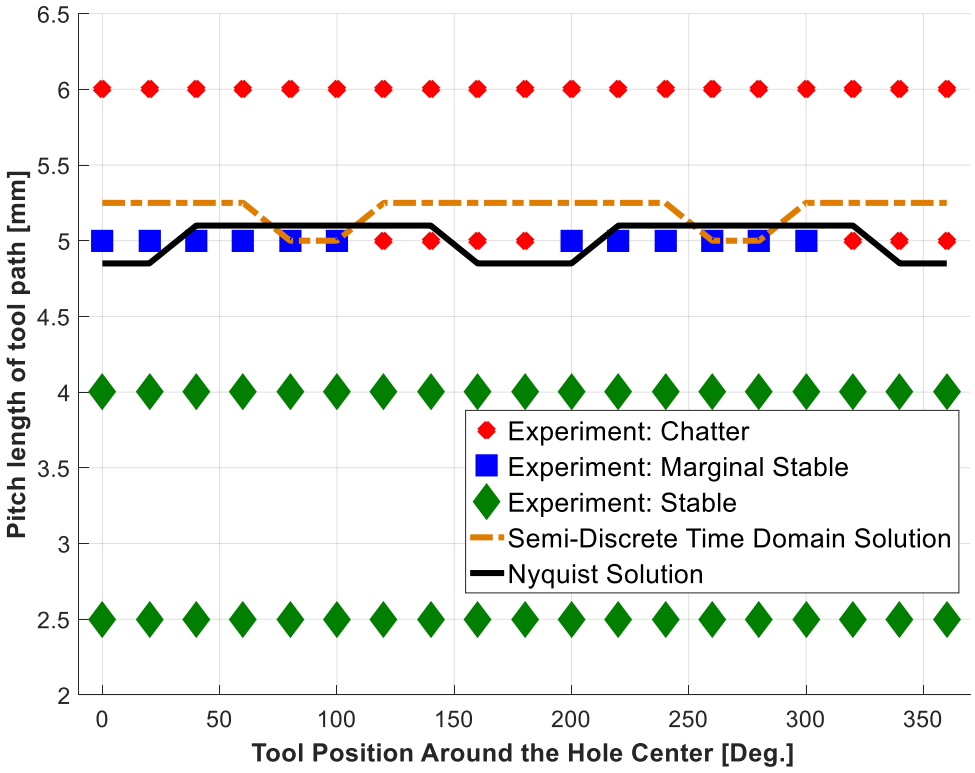

Figure 4.22 Stability limits during the rotation of the tool around the hole center for $\boldsymbol{n}$ = 9200 RPM

Chapter 5: Conclusion

5.1 Conclusions

The mechanics and dynamics of orbital drilling operations have been modeled in this thesis. The model is able to predict the cutting forces, chatter stability and dimensional hole quality for cylindrical helical end mills with drilling edges at their bottom.

The mechanics model uses orthogonal to oblique transformation at the helical flutes at the periphery of the end mill. The orthogonal model is based on the plastic shearing, and uses shear yield stress, shear angle and average Coulomb friction coefficient of the work-tool material couple. Due to indentation and severe ploughing, the orthogonal to oblique cutting model has shown to be unsuitable for the penetration of the bottom flutes into the material during downward motion, i.e. drilling with the end mill. The cutting force coefficients have been mechanistically identified from cutting tests, and used in modeling the contribution of the cutting forces by the cutting edges at the bottom face of the end mill.

The kinematic model of the orbital drilling motion has been modeled as a function of tool and hole geometries, spindle speed, tangential and orbital feed velocities. The distribution of chip thickness along the bottom and periphery of the end mill have been modeled, and used in predicting the vibration free (i.e. static) cutting forces. The model has led to accurate prediction of cutting forces quite well in lateral directions, but not well in the axial direction where the forces are dominated by ploughing due to plunging into the material.

The chatter stability model has been reduced to orbital feed independent, regular milling system by orienting the structural flexibilities in the feed and normal directions. The stability has been solved as a function of pitch length of the orbital motion in frequency domain using Nyquist Stability Criteria, and in Semi Discrete Time domain proposed by Insperger and Stepan. The predicted stability lobes have been experimentally proven on a mill turn machine tool.

The contributions of the thesis can be summarized as follows:

- A general force model of orbital drilling for cylindrical flat end mills is developed. A numerical model for calculating the TWE is introduced.
- The dynamic force model of orbital drilling that considers the vibration on lateral (x, y) and axial (z) directions is presented.
- The effect of orbital motion on time delay is analyzed and found to be negligible.
- Since the feed direction of the end mill is changing during orbital drilling, FRF on global coordinates projected along instantaneous feed and normal direction. Hence the stability charts are 3 dimensional considering the end mills position around the hole center, spindle speed and pitch length of the tool path.
- In frequency domain, Nyquist stability criterion is utilized in order to obtain accurate stable pitch lengths since the radial engagement conditions are not constant throughout the end mill diameter.

The proposed mathematical model has the following impact on the orbital drilling operations used in industry:

- The model allows the chatter free spindle speed, orbital feed and pitch length of the operation that leads to highest material removal rates.

- The prediction of cutting forces, hence the torque and power allows the selection of tool diameter and cutting conditions which do not violate the tool's breakage and machine tool's spindle's torque-power limits.

5.2 Future Research Directions

Future research directions can be pursued in following topics:

- The cutting coefficients related with the bottom part of the end mill are obtained by using the mechanistic approach in this thesis. However, the process is dominated by indentation mechanics which can be modeled based on slip line field or other plasticity methods.
- For high speed orbital drilling applications (i.e. robotic orbital drilling), the gyroscopic effects that might come from the orbital motion of the cutter could be analyzed.
- Orbital drilling is a highly used process in aerospace industry especially on difficult to cut materials at low spindle speeds. The modeling of process damping that considers the contact between the flank face of the cutting edge and cut surface is needed.
- Optimization of the orbital drilling process which considers structural dynamics of the machine, work material properties, Computer Numerical Control (CNC) servo drive bandwidth, tool breakage and dimensional hole surface errors can be highly useful tool for manufacturing industry.

Bibliography

[1] Lindqvist, Richard, Ingvar Eriksson, and Mathias Wolf. *Orbital drilling of sandwich constructions for space applications*. No. 2001-01-2571. SAE Technical Paper, 2001.

[2] Kihlman, Henrik, Ingvar Eriksson, and Mark Ennis. *Robotic orbital drilling of structures for aerospace applications*. No. 2002-01-2636. SAE Technical Paper, 2002.

[3] Lindqvist, Richard, and Henrik Kihlman. *Orbital drilling-implementation and evaluation*. No. 2004-01-2814. SAE Technical Paper, 2004.

[4] Whinnem, Eric. *Development and deployment of orbital drilling at Boeing*. No. 2006-01-3152. SAE Technical Paper, 2006.

[5] Iyer, R., P. Koshy, and E. Ng. "Helical milling: an enabling technology for hard machining precision holes in AISI D2 tool steel." *International Journal of Machine Tools and Manufacture* 47.2 (2007): 205-210.

[6] Denkena, Boehnke, D. Boehnke, and J. H. Dege. "Helical milling of CFRP–titanium layer compounds." *CIRP Journal of manufacturing Science and Technology* 1.2 (2008): 64-69.

[7] Marguet, Benoit, et al. *Advanced portable orbital-drilling unit for airbus final assembly lines*. No. 2007-01-3849. SAE Technical Paper, 2007.

[8] Brinksmeier, E., and S. Fangmann. "Burr and cap formation by orbital drilling of aluminum." *Burrs-Analysis, Control and Removal*. Springer Berlin Heidelberg, 2010. 31-45.

[9] Sadek, A., M. Meshreki, and M. H. Attia. "Characterization and optimization of orbital drilling of woven carbon fiber reinforced epoxy laminates." *CIRP Annals-Manufacturing Technology* 61.1 (2012): 123-126.

[10] Zhou, Lan, et al. "Hole diameter variation and roundness in dry orbital drilling of CFRP/Ti stacks." *The International Journal of Advanced Manufacturing Technology* 87.1-4 (2016): 811-824.

[11] Brinksmeier, Ekkard, Sascha Fangmann, and I. Meyer. "Orbital drilling kinematics." *Production engineering* 2.3 (2008): 277-283.

[12] Li, Zhongqun, and Qiang Liu. "Surface topography and roughness in hole-making by helical milling." *The International Journal of Advanced Manufacturing Technology* (2013): 1-11.

[13] Liu, Changyi, Gui Wang, and Matthew S. Dargusch. "Modelling, simulation and experimental investigation of cutting forces during helical milling operations." *The International Journal of Advanced Manufacturing Technology* 63.9 (2012): 839-850.

[14] Wang, Haiyan, et al. "Prediction of cutting forces in helical milling process." *The International Journal of Advanced Manufacturing Technology* 58.9 (2012): 849-859.

[15] Rey, P. A., et al. "Modelling of cutting forces in orbital drilling of titanium alloy Ti–6Al–4V." *International Journal of Machine Tools and Manufacture* 106 (2016): 75-88

[16] Li, Zhongqun, et al. "Cutting force prediction and analytical solution of regenerative chatter stability for helical milling operation." *International Journal of Advanced Manufacturing Technology* 73 (2014).

[17] Kardes, N., and Y. Altintas. "Mechanics and dynamics of the circular milling process." *Journal of manufacturing science and engineering* 129.1 (2007): 21-31.

[18] Wan, Min, and Yusuf Altintas. "Mechanics and dynamics of thread milling process." *International Journal of Machine Tools and Manufacture* 87 (2014): 16-26.

[19] Insperger, Tamás, and Gábor Stépán. "Updated semi-discretization method for periodic delay-differential equations with discrete delay." *International Journal for Numerical Methods in Engineering* 61.1 (2004): 117-141.

[20] Armarego, E. J. A., and R. C. Whitfield. "Computer based modelling of popular machining operations for force and power prediction." *CIRP Annals-Manufacturing Technology* 34.1 (1985): 65-69.

[21] Pirtini, M., and I. Lazoglu. "Forces and hole quality in drilling." *International journal of machine tools and Manufacture* 45.11 (2005): 1271-1281.

[22] Roukema, Jochem C., and Yusuf Altintas. "Generalized modeling of drilling vibrations. Part I: Time domain model of drilling kinematics, dynamics and hole formation." *International Journal of Machine Tools and Manufacture* 47.9 (2007): 1455-1473.

[23] Ema, S., and E. Marui. "Theoretical analysis on chatter vibration in drilling and its suppression." *Journal of Materials Processing Technology* 138.1 (2003): 572-578.

[24] Roukema, Jochem C., and Yusuf Altintas. "Generalized modeling of drilling vibrations. Part II: Chatter stability in frequency domain." *International Journal of Machine Tools and Manufacture* 47.9 (2007): 1474-1485.

[25] Bayly, Philip V., et al. "Theory of torsional chatter in twist drills: model, stability analysis and composition to test." *Journal of manufacturing science and engineering* 123.4 (2001): 552-561.

[26] Ahmadi, K., and Y. Altintas. "Stability of lateral, torsional and axial vibrations in drilling." *International Journal of Machine Tools and Manufacture* 68 (2013): 63-74.

[27] Altintaş, Y., and E. Budak. "Analytical prediction of stability lobes in milling." *CIRP Annals-Manufacturing Technology* 44.1 (1995): 357-362.

[28] Bayly, P. V., et al. "Stability of interrupted cutting by temporal finite element analysis." *Journal of Manufacturing Science and Engineering* 125.2 (2003): 220-225.

[29] Eksioglu, C., Z. M. Kilic, and Y. Altintas. "Discrete-time prediction of chatter stability, cutting forces, and surface location errors in flexible milling systems." *Journal of Manufacturing Science and Engineering* 134.6 (2012): 061006.

[30] Ko, Jeong Hoon, and Yusuf Altintas. "Time domain model of plunge milling operation." *International Journal of Machine Tools and Manufacture* 47.9 (2007): 1351-1361.

[31] Altintas, Y., and E. J. A. Armarego. "Prediction of milling force coefficients from orthogonal cutting data." *Trans. ASME J. Engng Ind* (1996).

[32] Altintas, Yusuf. *Manufacturing automation: metal cutting mechanics, machine tool vibrations, and CNC design*. Cambridge university press, 2012.

[33] Long, X-H., B. Balachandran, and B. P. Mann. "Dynamics of milling processes with variable time delays." *Nonlinear Dynamics* 47.1 (2007): 49-63

[34] Altintas, Y., and E. Budak. "Analytical prediction of chatter stability in milling—part I: general formulation." *Journal of Dynamic Systems, Measurement, and Control* 120 (1998): 22-30

[35] Yanushevsky, B. "A new theoretical approach for the prediction of machine tool chatter in milling." *Journal of engineering for industry* 115 (1993): 1.

[36] Wereley, Norman M. *Analysis and control of linear periodically time varying systems*. Diss. Massachusetts Institute of Technology, 1990.

[37] Govekar, E., et al. "On stability and dynamics of milling at small radial immersion." *CIRP Annals-Manufacturing Technology* 54.1 (2005): 357-362.

[38] Insperger, Tamás, and Gábor Stépán. "Stability of the milling process." *Periodica Polytechnica. Engineering. Mechanical Engineering* 44.1 (2000): 47.

[39] Altintas, Y., and Z. M. Kilic. "Generalized dynamic model of metal cutting operations." *CIRP Annals-Manufacturing Technology* 62.1 (2013): 47-50.

[40] Koenisberger, F., and J. Tlusty. "Machine Tool Structures-Vol. I: Stability Against Chatter." (1967): 202-203.